Master Thesis

Investigating Gamma-ray Emission from the Dragonfly Pulsar and the Geminga Pulsar with MAGIC Observations

Department of Physics
Ludwig-Maximilians-Universität München

Yunhe Wang

Munich, Feb 14th, 2025

Supervised by PD Dr. Gayoung Chon

Masterarbeit

Untersuchung der Gammastrahlenemission des Dragonfly-Pulsars und des Geminga-Pulsars mit MAGIC-Beobachtungen

Fakultät für Physik
Ludwig-Maximilians-Universität München

Yunhe Wang

München, 14. Februar, 2025

Betreut von PD Dr. Gayoung Chon

Declaration of Authorship

I hereby declare that this thesis is my own work, and that I have not used any sources and aids other than those stated in the thesis.

Munich, 14 Feb 2025, Yunhe Wang

Declaration of AI Usage

I declare that I have exclusively used ChatGPT 4 (and/or any other AI tool, if applicable) in my thesis/paper for the purposes listed below:
E.g.
• Brainstorming on my topic
• Correction of grammar, proof reading and editing
Prompts are available in the AI Usage Reflection.
I confirm that I have checked my thesis and its text for unintended plagiarism and that I have verified all facts and references used from the ChatGPT output.

Munich, 14 Feb 2025, Yunhe Wang

Abstract

Very-high-energy observations of pulsars provide unique insights into the most energetic radiation processes in the pulsar magnetosphere. With observations from the Major Atmospheric Gamma Imaging Cherenkov (MAGIC) telescopes, this thesis investigates the gamma-ray emissions from two pulsars: the Dragonfly pulsar (PSR J2021+3651), whose pulsed emissions at energies above $\sim 30\,\mathrm{GeV}$ were searched in the MAGIC archival data, and the Geminga pulsar (PSR J0633+1746), whose spectral features were cross-checked with a different method.

The analysis was performed using the existing pulsar analysis pipeline, complemented by a spectral-analysis technique implemented in this work, the Markov Chain Monte Carlo (MCMC) analysis with Tikhonov regularization. While the study of the Dragonfly pulsar relied on the MAGIC Analysis and Reconstruction Software (MARS) and non-standard procedures specialized for low-energy data, the spectral analysis of Geminga was performed using `Gammapy`, the official scientific tool for the Cherenkov Telescope Array Observatory (CTAO), the next-generation observatory in the very-high-energy (VHE) gamma-ray astronomy. Testing the performance of `Gammapy` for low-energy pulsar data is important for future analysis. This work identified issues with flux point estimation in `Gammapy`, implemented the MCMC technique with Tikhonov regularization to overcome the ill-posed nature of this problem, and obtained robust estimates of spectral points.

For the Dragonfly pulsar, we searched for the pulsed gamma-ray emissions in the $30\,\mathrm{GeV}$ to $200\,\mathrm{GeV}$ energy range. No significant pulsed component was detected, with very low significance of $\sim 1\sigma$ in different statistical tests. This result could indicate the possibility that the Dragonfly pulsar inherently does not produce VHE gamma-ray pulsations, or it could also be due to the limited observation time.

For the Geminga pulsar, the spectral results obtained using `Gammapy` and the MCMC-based method are consistent with previous MARS analysis. The spectrum is described by a power-law model with a spectral index of $\Gamma = 5.17 \pm 0.39$, and no preference for a curved spectrum was found. This confirmed the presence of a power-law tail in the high-energy emission of Geminga, as revealed by previous MAGIC analysis, implying that an inverse Compton process occurs in the pulsar magnetosphere.

Contents

Chapter 1

Introduction

Pulsars are rapidly rotating neutron stars (NS) with radiation beam periodically sweeping across the line of sight of an observer. The hypothesis of the presence of neutron star, a kind of compact star supported by the degenerate pressure of neutrons and formed after supernova explosion, was proposed by Landau (1932) and Baade and Zwicky (1934), long before the discovery of the first radio pulsar by Hewish et al. (1968).

Pulsars are ideal targets to study the physics under extreme conditions. Formed after the supernova explosion of a massive star ($8\,\mathrm{M}_\odot \lesssim M \lesssim 20\,\mathrm{M}_\odot$), they have a typical mass of $\sim 1.4\ \mathrm{M}_\odot$ and a radius of $\sim 10\,\mathrm{km}$, which is only about three times of the Schwarzschild radius. At only about 0.5 km below the surface, the density reaches $\sim 10^{14}\,\mathrm{g\,cm^{-3}}$, the density of nuclear matter. Studying the structure of pulsars provides insights into the nature of the strong interaction and the properties of matter at extremely high densities. The strong magnetic fields, with a typical order of magnitude of $10^{12}\,\mathrm{G}$, play an important role in the formation of the pulsar magnetosphere, a surrounding plasma mainly filled with electron and positron pairs. Complex radiation processes occur in the magnetosphere, leading to the multi-wavelength emissions observed in radio, X-ray, and very high energy (VHE) bands.

Observations of gamma-ray pulsars have entered a new era with the launch of *Fermi* Large Area Telescope (LAT), expanding the number of known gamma-ray pulsars from 6 in the EGRET observations (Thompson, 2008) to nearly 300 (Smith et al., 2023). While the spectral features in the energy range of $\sim 100\,\mathrm{MeV}$ to tens of GeV have become clear, the gamma-ray emissions at VHE energies are not fully understood, due to the very small number of sources detected by the Imaging Atmospheric Cherenkov Telescopes (IACTs).

This chapter introduces the theoretical framework and observational strategies of the very high energy gamma-ray emissions from pulsars. Sec. 1.1 discusses basic physical properties of pulsars, with a focus on the pulsar magnetosphere, which is closely related to the high-energy emission. Sec. 1.2 describes the detection technique for VHE gamma-rays,

and introduces the instruments of the Major Atmospheric Gamma Imaging Cherenkov (MAGIC) telescopes used for the observations in this work. Sec. 1.3 reviews previous multi-wavelength observations of the Dragonfly pulsar and the Geminga pulsar, whose VHE gamma-ray emissions are studied in this thesis.

1.1 Gamma-ray pulsars

This section presents the theoretical framework for the pulsar magnetosphere and the high-energy emissions. Sec. 1.1.1 introduces basic pulsar properties in the framework of magnetic dipole model, in particular the surface magnetic field strength and the characteristic age. Based on the the structure of the pulsar magnetosphere provided in Sec. 1.1.2, Sec. 1.1.3 discusses the gamma-ray emission mechanisms and possible particle acceleration models.

1.1.1 Properties of pulsars

The magnetic dipole model, a simple model that describes a pulsar as a magnetized sphere rotating in the vacuum, is essential to understand the basic physical properties of the rotation-powered pulsars.

In the magnetic dipole model, the pulsar rotates with an angular frequency $\Omega = 2\pi/P$, and has a magnetic moment $\boldsymbol{\mu}$ inclined to the spin axis with an angle α. The radiation power from the rotating magnetic dipole is given by

$$\dot{E}_d = -\frac{2}{3c^3}|\boldsymbol{\mu}|^2\Omega^4 \sin^2\alpha \ . \tag{1.1}$$

The magnetic dipole radiation is derived from the loss of the rotational energy, which can be expressed as

$$\dot{E}_r = \frac{\mathrm{d}(I\Omega^2/2)}{\mathrm{d}t} = -I\Omega\dot{\Omega} = 4\pi^2 I\frac{\dot{P}}{P^3} \ , \tag{1.2}$$

where I is the moment of inertia, P is the rotational period, and $\dot{P} = \mathrm{d}P/\mathrm{d}t$ represents the increase of pulsar period with time, known as the spin-down process.

This model assumes the spin-down process is mainly due to magnetic dipole radiation,

$$\dot{E}_r = \dot{E}_d \ . \tag{1.3}$$

By relating the magnetic moment with the magnetic field strength $|\boldsymbol{\mu}| \simeq Br^3$, we can estimate the magnetic field strength at the pulsar surface

$$B_s(r = R) = \frac{1}{\sin\alpha}\sqrt{\frac{3Ic^3P\dot{P}}{8\pi^2R^6}} \ . \tag{1.4}$$

For a neutron star with a characteristic radius of $R \simeq 10$ km and a mass of $M \simeq 1.4$ $M_\odot$, the moment of inertia can be estimated as $I = \frac{2}{5}MR^2 \simeq 10^{45}$ g cm^2. Using these values, we can estimate the surface magnetic field strength from the two observables P and $\dot{P}$:

$$B_s \simeq 10^{12} \text{ G} \left(\frac{\dot{P}}{10^{-15}}\right)^{\frac{1}{2}} \left(\frac{P}{s}\right)^{\frac{1}{2}} . \tag{1.5}$$

From Eq. 1.3 we can also establish the relation between $\dot{P}$ and P. Integrating it we obtain the characteristic age of pulsars,

$$\tau_c = \frac{P}{2\dot{P}} \simeq 15.8 \text{ Myr} \left(\frac{P}{s}\right) \left(\frac{\dot{P}}{10^{-15}}\right)^{-1} . \tag{1.6}$$

In conclusion, assuming that the spin-down process is due to magnetic dipole radiation in the vacuum, the magnetic dipole model provides estimates of the surface magnetic field strength and characteristic age of pulsars from observables P and $\dot{P}$. This allows us to understand the spin evolution in the $P - \dot{P}$ diagram.

Fig. 1.1 shows the pulsar $P - \dot{P}$ diagram using data from the ATNF Pulsar Catalog[1] (Manchester et al., 2005). The dashed lines represent the constant characteristic age and magnetic field strength. In general, there are two distinct populations of high-energy, gamma-ray emitting pulsars: 1) the millisecond pulsars ($P \sim 3$ ms): very old pulsars in a binary system, whose rotation is spun up by the mass transfer from its companion star. 2) the rotation-powered pulsars ($P \sim 0.5$ s): the young pulsars have large magnetic field and spin-down rate, while the intermediate-aged and old pulsars are characterized by weaker magnetic field and lower spin-down rate. The Dragonfly pulsar and the Geminga pulsar studied in this work belong to the latter category, and are highlighted in this diagram.

1.1.2 Pulsar magnetosphere

As is shown in Goldreich and Julian (1969), a rotating, magnetized neutron star in a vacuum is an unstable state that cannot be maintained in reality. Their results provide insights into the surrounding region of the neutron star, where the observed radiation originates, and are therefore summarized here.

Assuming the neutron star is a perfect conductor, the electric field inside the star will balance the induced electric field produced by the rotating magnetized sphere

$$\boldsymbol{E}^{\text{in}} + (\boldsymbol{\Omega} \times \boldsymbol{r}) \times \boldsymbol{B} = 0 . \tag{1.7}$$

[1] `https://www.atnf.csiro.au/research/pulsar/psrcat/`

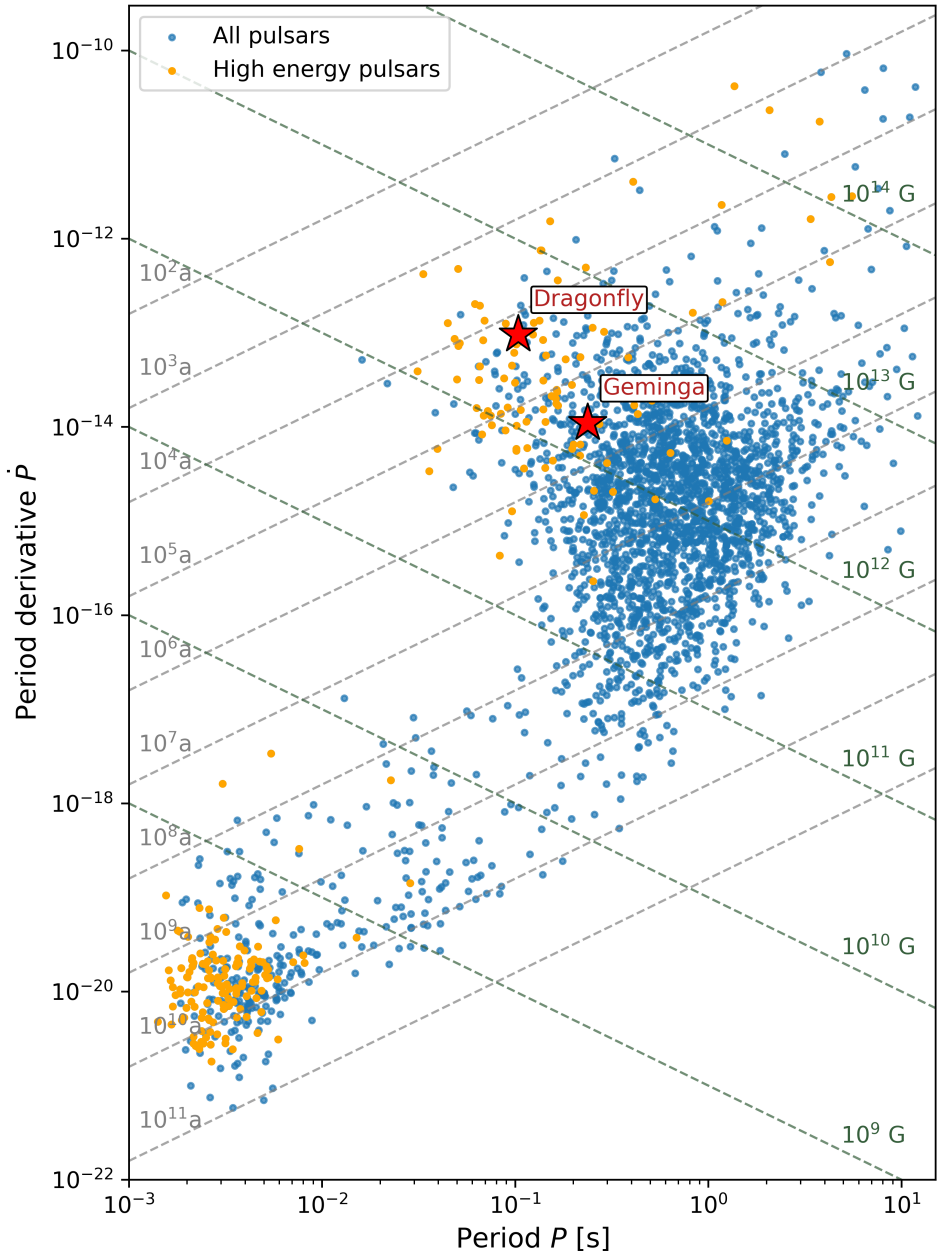

Figure 1.1: The pulsar $P-\dot{P}$ diagram, produced using data from the ATNF Pulsar Catalog (Manchester et al., 2005). The high-energy pulsars are shown in yellow. The dashed lines represent the constant characteristic age and magnetic field strength, calculated by Eq. 1.6 and Eq. 1.5, respectively. There are two distinct classes: the millisecond pulsars (left corner) and the rotation-powered pulsars (upper right) (see text for details). The Dragonfly pulsar and the Geminga pulsar studied in this work are highlighted in this diagram.

Solving Poisson's equation in the vacuum ($\nabla^2\Phi = 0$) gives the external electrostatic potential

$$\Phi = \frac{-B_0 \Omega R^5}{3cr^3} P_2(\cos\theta) \ , \tag{1.8}$$

where B_0 is the polar magnetic field, P_2 is the second Legendre polynomial, and r, θ, ϕ are the spherical coordinates.

Then, the component of the *external* electric field parallel to the the magnetic dipole field $E_\parallel$ can be determined from

$$\boldsymbol{E} \cdot \boldsymbol{B} = -\left(\frac{\Omega R}{c}\right)\left(\frac{R}{r}\right)^7 B_0^2 \cos^3\theta \ . \tag{1.9}$$

For characteristic pulsar parameters $R \simeq 10$ km, $\Omega \simeq 10$ Hz, $B_0 \simeq 10^{12}$ G, the order of magnitude of $E_\parallel$ is approximately 10^{13} V/m in the vacuum model.

Such large parallel electric field can easily overcome the gravitational attraction, extracting charges from the surface, leading to the formation of a surrounding plasma, which is the pulsar *magnetosphere*.

The surrounding magnetosphere co-rotates with the neutron star, extending to the radius at which the co-rotational velocity equals to the speed of light:

$$r_L = \frac{c}{\Omega} \ , \tag{1.10}$$

which defines the region of *light cylinder*.

A schematic of the structure of the pulsar magnetosphere is shown in Fig. 1.2. Inside the light cylinder, particles co-rotate and move along the *closed field lines*. In the *open field line* region, where the field lines cross the light cylinder and extend to infinity, the ultra-relativistic charges flow out from the magnetosphere, stream away to infinity, and form the pulsar wind. The region where all open magnetic field lines intersect the star's surface defines the pulsar *polar cap*.

In the co-rotating magnetosphere, the local charge density is given by

$$\rho_{\rm GJ} = \frac{\nabla \cdot \boldsymbol{E}}{4\pi} = -\frac{\boldsymbol{\Omega} \cdot \boldsymbol{B}}{2\pi c} \frac{1}{1 - (\Omega r/c)^2 \sin^2\theta} \ , \tag{1.11}$$

which is known as the Goldreich-Julian charge density. It corresponds to an equilibrium where the electric field balances the Lorentz force. In other words, the parallel electric field is screened by the redistributed particles in the ideal plasma. Any deviation of the charge distribution from ρ_{GJ} will lead to a net imbalance between the Lorentz force and the electric field that can accelerate charges.

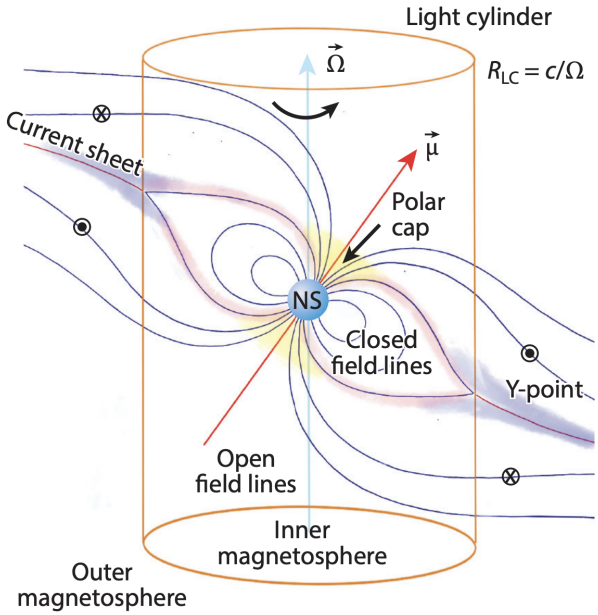

Figure 1.2: Basic structure of the pulsar magnetosphere and the locations of the emissions, fromPhilippov and Kramer (2022).

1.1.3 High-energy emission

With the physical picture of the pulsar magnetosphere structure, this section discusses the basic emission mechanisms and possible particle acceleration locations. I refer the reader to a recent review Philippov and Kramer (2022) for a state-of-the-art discussion of magnetosphere physics.

There are three basic processes for the production of high-energy photons in the magnetosphere: 1) *synchrotron radiation* produced by ultra-relativistic electrons spiraling around the magnetic field line; 2) *curvature radiation* from electrons moving along a curved magnetic field line in a strong magnetic field; 3) *inverse Compton scattering* of a lower-energy photon by a high-energy electron. The lower-energy photons can be synchrotron photons or the hard X-ray photons from the thermal emission from the pulsar surface.

The spectral shapes of these radiation processes depend on the underlying electron distribution. For a power law energy distribution of electrons $N_e(\gamma) = \gamma^{-\alpha}$, the spectrum of inverse Compton scattering is a power-law with an index of $\Gamma = \alpha + 1$, in the regime where the energy of the scattering electrons is much larger than that of the seed photons. The spectra of synchrotron radiation and curvature radiation are characterized by a power-law component with different indexes, $\Gamma_{\rm curv} = (\alpha + 2)/3$ and $\Gamma_{\rm sync} = (\alpha + 1)/2$, with an exponential cut-off at high energies (see Ceribella (2021) for a detailed derivation).

While the basic emission processes are relatively clear, the location where the high-energy

emissions are produced is not fully understood. The polar cap model is an early classic model (Sturrock, 1971; Ruderman and Sutherland, 1975; Daugherty and Harding, 1996). In the polar cap model, electrons are accelerated by the electric field in a vacuum gap near the surface of the polar cap region, producing gamma-ray photons through curvature radiation. However, in the presence of the strong surface magnetic field, the high-energy photons will be absorbed and produce electro-positron pairs, resulting in a super-exponential cut-off with cut-off index $\beta > 1$ in the spectrum. This model is not favored by observations, as the super-exponential cut-off is not generally observed in gamma-ray pulsars (e.g., Aliu et al. 2008), suggesting the outer regions are more likely to be the locations for high-energy emissions.

In the outer gap model, first proposed by Cheng et al. (1986), the vacuum gaps form in the outer region of the pulsar magnetosphere near the light cylinder. The electrons accelerated in these gaps emit gamma-rays through the combined process of synchro-curvature radiation and inverse Compton scattering. This model is widely considered to account for the spectral features of gamma-ray pulsars in the EGRET observations (Romani, 1996) and *Fermi*-LAT observations (Abdo et al., 2010a,b,c). However, the VHE spectrum of the Geminga pulsar can not be fully explained by the outer gap model (MAGIC Collaboration, 2020), indicating modifications of existing theories are required.

Among various possible acceleration regions, the equatorial current sheet is a promising origin of the observed gamma-rays. As is illustrated in Fig. 1.2, there is a Y-shape current sheet in the equatorial plane. This feature is revealed by early numerical solutions (Contopoulos et al., 1999; Gruzinov, 2005; Timokhin, 2006) and further studied in the particle-in-cell (PIC) simulations of plasmas (Kalapotharakos et al., 2018; Guépin et al., 2020). By modeling particle acceleration in the current sheet, the spectra constructed from PIC simulations are generally in agreement with Fermi observations (Cerutti et al., 2016; Philippov and Kramer, 2022).

While hundreds of gamma-ray pulsars have been detected by *Fermi*-LAT, only three pulsars have been observed in the VHE band with high significance: the Crab (Aliu et al., 2008), the Vela (H.E.S.S. Collaboration, 2018), and the Geminga (MAGIC Collaboration, 2020). To distinguish between different particle acceleration models, measuring the spectral features at higher energies is crucial. With observations of more pulsars from IACTs, our understanding of the gamma-ray emission mechanisms in the magnetosphere will be greatly improved in the future.

1.2 Detection of the very high energy gamma-rays

This section introduces the detection technique of the imaging atmospheric Cherenkov telescopes and the instruments of the MAGIC telescopes. The interactions of VHE photons with the atmosphere and the resulting particle cascades are introduced in Sec. 1.2.1.

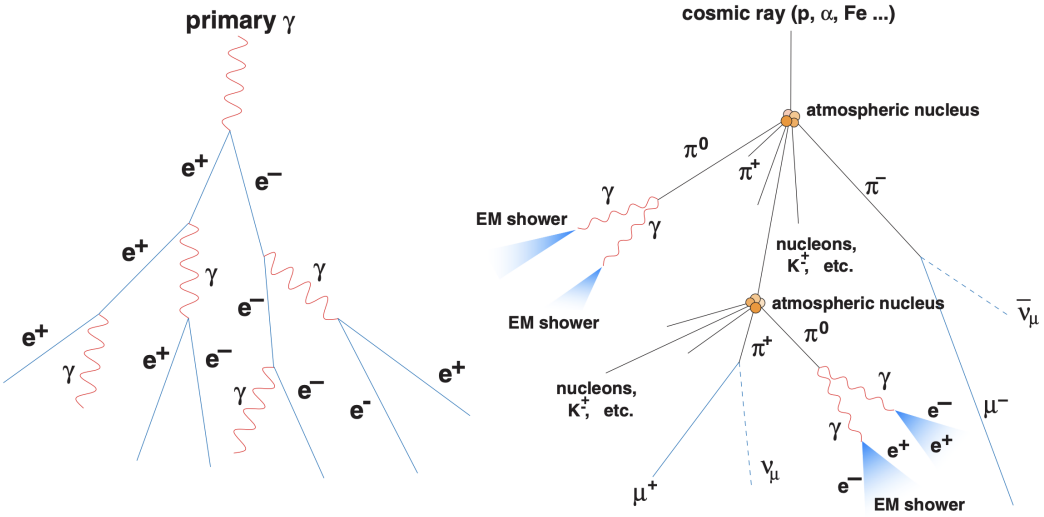

Figure 1.3: Schematic of extensive air showers, from Wagner (2006). Left: electromagnetic shower. Right: hadronic shower.

Sec. 1.2.2 discusses the Cherenkov light produced by these particles, which can be collected by IACTs. Sec. 1.2.3 focuses on the MAGIC telescopes used for the observations in this work.

1.2.1 Extensive air showers

When a very high energy (VHE) primary particle enters the earth's atmosphere, it will interact with the air nuclei in a series of repeated interactions, and produce cascades of new particles. These particle cascades, known as the extensive air showers (EAS), were first discovered by Rossi (1934) and explained by Auger et al. (1939). Depending on the type of the primary particle, air showers can be divided into two categories: electromagnetic showers and hadronic showers, induced by VHE gamma-rays and comic rays, respectively (Fig. 1.3).

The main processes in an electromagnetic shower are pair production and Bremsstrahlung. A high-energy photon produces an electron-positron pair in the field of the air nuclei. The created electron and positron will further radiate photons via Bremsstrahlung. The two processes will repeat, creating cascades of gamma-rays, electrons and positrons. As the electromagnetic shower develops, the number of charged particles rapidly increases at the early stage, reaches a maximum (shower maximum), and then decreases due to the low average energy of particles. When the average energy drops below the threshold $E_c \simeq 85\,\mathrm{MeV}$, the energy loss of electrons due to ionization becomes more dominant than the loss from Bremsstrahlung, and gamma-ray photons can not be further produced. The development of an electromagnetic shower depends on the energy of the primary gamma-

ray. Air showers induced by photons with higher energy have longer propagation length and larger value of shower maximum.

More complicated processes are involved in the formation of hadronic showers. Due to the complexities in modeling strong interactions, detailed studies of hadronic showers rely on the measurements of the forward cross-section performed with collider experiments. The basic processes are illustrated in Fig. 1.3. When a cosmic-ray particle interacts with the air nuclei, it will produce kaons, charged and neutral pions. The neutral pions will decay into two photons

$$\pi^0 \to \gamma + \gamma \ , \tag{1.12}$$

which further induce electromagnetic showers. The charged pions decay into muons and neutrinos,

$$\begin{aligned} \pi^+ &\to \mu^+ + \nu_\mu \\ \pi^- &\to \mu^- + \bar{\nu}_\mu \ , \end{aligned} \tag{1.13}$$

which continue to propagate without significant interactions. The remaining hadronic components will further interact with atmosphere, producing secondary kaons and pions, and continuing the development of the hadronic cascade.

1.2.2 Cherenkov radiation

A main way to detect the extensive air showers is through observations of the Cherenkov light from the shower particles.

Cherenkov radiation can be produced when a charged particle travels through a medium with a velocity larger than the speed of light in the medium,

$$v = \beta c > \frac{c}{n} \ , \tag{1.14}$$

where n is the refractive index of the medium. This effect is related to the depolarization of the medium. A charged particle will polarize the surrounding particles in the medium. If $v < c/n$, the symmetrically polarized particles will be symmetrically distributed, and the dipole radiations from the depolarization process will result in no emission. If $v > c/n$, the polarized particles will be asymmetrically distributed after the moving particle, and their depolarization will produce a cone-like radiation. The angle between the radiation and the direction of particle motion is

$$\cos\theta = \frac{1}{n\beta} \ . \tag{1.15}$$

In the atmosphere, the threshold for Cherenkov radiation is about $E_c \simeq 20\,\mathrm{MeV}$ at the sea level, smaller than the energy threshold for the electromagnetic showers. Therefore, all

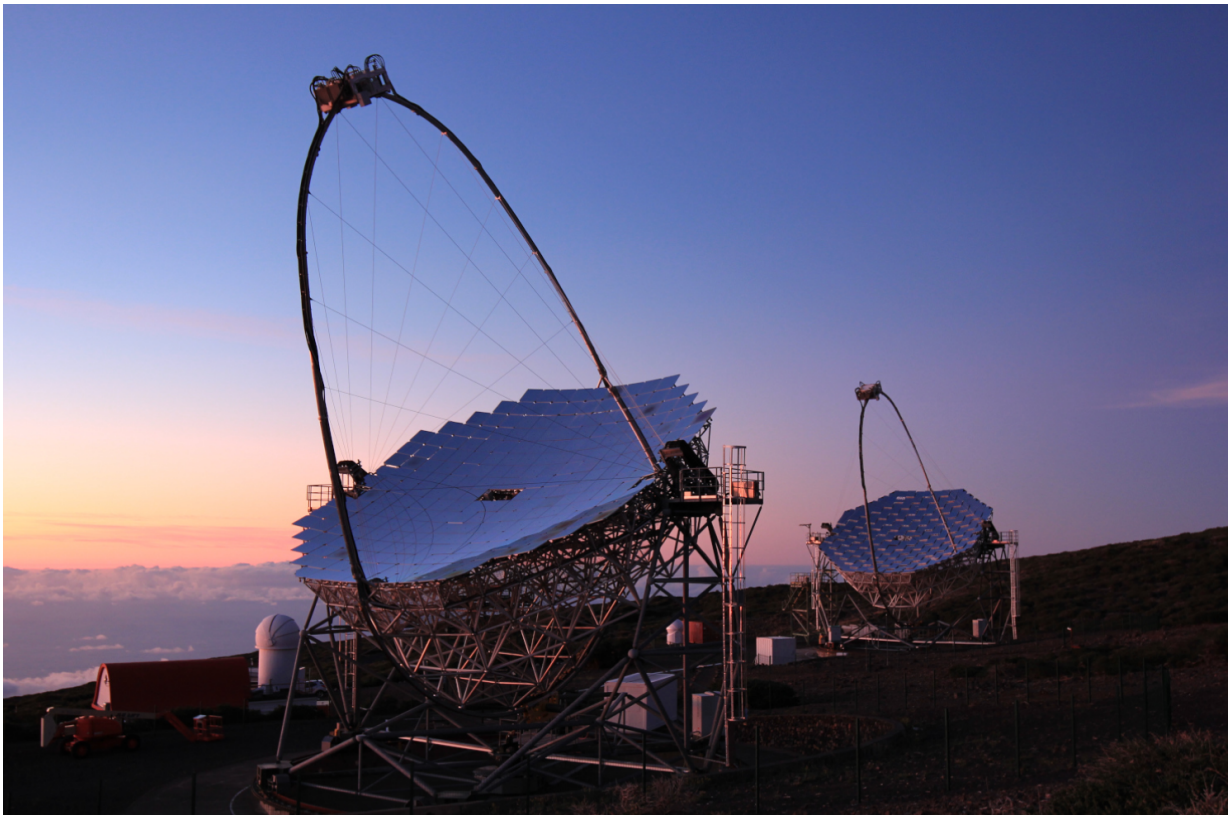

Figure 1.4: Picture of the MAGIC telescopes with MAGIC-II in the front, and MAGIC-I in the back. (credit: G. Ceribella / MPI)

electrons and positrons in the shower will produce Cherenkov radiation, the total intensity of Cherenkov light is proportional to the number of charged particles, and correspondingly, proportional to the energy of the primary particle. Furthermore, considering the emission angle of the Cherenkov radiation, the total Cherenkov light will cover a limited area on the ground (light pool), and be detected by the imaging atmospheric Cherenkov telescopes.

1.2.3 The MAGIC telescopes

The MAGIC telescopes consist of two imaging atmospheric Cherenkov telescopes located at the Roque de los Muchachos Observatory on the Canary Island of La Palma, at an altitude of 2200 m. The observations of the first telescope began in 2014, while the second telescope was operating since 2009, with a separation of 85 m from MAGIC-I (Fig. 1.4). The two telescopes enable stereo-observations, which helps to determine the incoming direction of the primary particle. The MAGIC telescopes operate in the energy range from few tens of GeV to $\sim$ 100 TeV, allowing the study of very-high-energy gamma-rays from various galactic and extragalactic sources.

Reflector

The reflector has a diameter of 17 m, with a focal to diameter ratio $f/D = 1.03$. It has a parabolic shape, designed to maintain the time structure of the short (1-3 ns) Cherenkov flash. The reflective surface of each MAGIC telescope is composed of movable $1\,\mathrm{m}^2$-sized mirror panels, with a total area of $236\,\mathrm{m}^2$. There are generally two types of mirror designs: the all-aluminum mirrors and the glass mirrors with front-coated aluminum layer (Doro et al., 2008). The reflecting aluminum layer is chosen for its high reflectivity in the peak wavelength range of the Cherenkov spectrum ($\sim 350\,\mathrm{nm}$), and is protected by a thin quartz coating from oxidation. The orientation of each mirror panel is automatically adjusted by an active mirror control system (Biland et al., 2008), in order to improve the *optical* point spread function (PSF) at different zenith angles, which is different from the gamma-ray PSF in the analysis.

Camera

The camera has a total field of view (FoV) of 3.5°, with each pixel contributing 0.1°. It consists of 1039 photomultiplier tubes (PMTs), uniformly arranged in a hexagonal grid, forming a circle of about 1 m diameter. The PMT is chosen as the light sensor for its sensitivity to single photons and fast response to the Cherenkov signal. The Hamamatsu R10408 PMTs used in MAGIC have a response time of $\sim 1\,\mathrm{ns}$ (FWHM) and a peak quantum efficiency (QE) of 34% (Borla Tridon et al., 2009; Nakajima et al., 2013).

1.3 Pulsars studied in this work

1.3.1 The Dragonfly pulsar

The Dragonfly pulsar (PSR J2021+3651) is an intermediate-aged pulsar, with a rotation period of $P = 103.7\,\mathrm{ms}$ and a spin-down rate $\dot{P} = 9.563 \times 10^{-14}$. This corresponds to a characteristic age $\tau_c \simeq 17\,\mathrm{kyr}$, a surface dipole magnetic field $B_s \simeq 3.2 \times 10^{12}\,\mathrm{G}$ and a spin-down luminosity $\dot{E}_r \simeq 3.4 \times 10^{36}\,\mathrm{erg\,s^{-1}}$.

Discovery of PSR J2021+3651

The radio pulsar PSR J2021+3651 was first discovered by Roberts et al. (2002) during the identification of EGRET gamma-ray sources. They targeted potential X-ray counterparts in the ASCA catalog for the unidentified EGRET sources, and searched for radio pulsations using Arecibo and Parkes telescopes. This led to the discovery of an intermediate-aged and energetic pulsar, PSR J2021+3651, which is associated with the X-ray source AX

J2021.1+3651 and the COS-B gamma-ray source 2CG 075+00. The pulsar parameters were measured and derived from radio observations. They are very similar to those of the Vela pulsar, which has a period of $P = 89.3\,\mathrm{ms}$ and a spin-down luminosity of $\dot{E}_r \simeq 6.9 \times 10^{36}\,\mathrm{erg\,s^{-1}}$. The main different parameter is the distance. The distance of the Vela pulsar, derived from parallax measurements, is $287^{+18}_{-19}\,\mathrm{pc}$ (Dodson et al., 2003). The distances of the Dragonfly pulsar determined from different methods are under debated, ranging from$\sim 2\,\mathrm{kpc}$ (Kirichenko et al., 2015), $\sim 5\,\mathrm{kpc}$ (Van Etten et al., 2008; Abdo et al., 2009), to $\sim 10\,\mathrm{kpc}$ (Roberts et al., 2002; Hessels et al., 2004).

X-ray observations and the Dragonfly nebula

The pulsar wind nebula (PWN) of PSR J2021+3651 was first revealed with Chandra observations, and named as G75.2+0.1 (Hessels et al., 2004). Its X-ray spectrum is well described by an absorbed power-law with a photon index of $\Gamma \simeq 1.7$, a hydrogen column density $N_H \simeq 7.8 \times 10^{21}\,\mathrm{cm^{-2}}$, and an unabsorbed flux of $F_{(0.5-10\,\mathrm{keV})} \simeq 1.7 \times 10^{12}\,\mathrm{ergs\,cm^{-2}\,s^{-1}}$. The thermal emission from the pulsar was also found, with a blackbody temperature of $T \simeq 0.15\,\mathrm{keV}$. The X-ray pulsations were also investigated in this study, and a low significance of 3.7σ was found.

The inner structure of the nebula was resolved by deeper Chandra exposure (Van Etten et al., 2008). As is shown in Fig. 1.5, the pulsar wind nebula has a double ridge structure and a narrow outer jet. With a morphology resembling a dragonfly, it is named the 'Dragonfly nebula', which also gives the name of the corresponding pulsar.

Pulsed gamma-ray emissions with AGILE and *Fermi*-LAT

The gamma-ray pulsations from the Dragonfly pulsar were discovered in the 100-1500 MeV range using data from the AGILE satellite, folded on a radio ephemeris obtained at the Green Bank Telescope (GBT) (Halpern et al., 2008). The gamma-ray phaseogram, a histogram of event counts binned by pulsar phase, consists of two sharp peaks (Fig. 1.6).

The pulsed gamma-rays from this pulsar were further studied with the first year Fermi-LAT observations from 0.1 GeV to more than 3 GeV energy (Abdo et al., 2009). The average spectrum is well described by an exponential cut-off power law, with photon index $\Gamma \simeq 1.5$ and the cut-off energy $E_c \simeq 2.4\,\mathrm{GeV}$. Gamma-ray emission from the polar cap region was considered the least likely explanation. In the third *Fermi*–LAT pulsar catalog, a sub-exponential cutoff was found with photon index $\Gamma \simeq 0.99 \pm 0.1$ and sub-exponential index $b = 0.25 \pm 0.06$ (Smith et al., 2023).

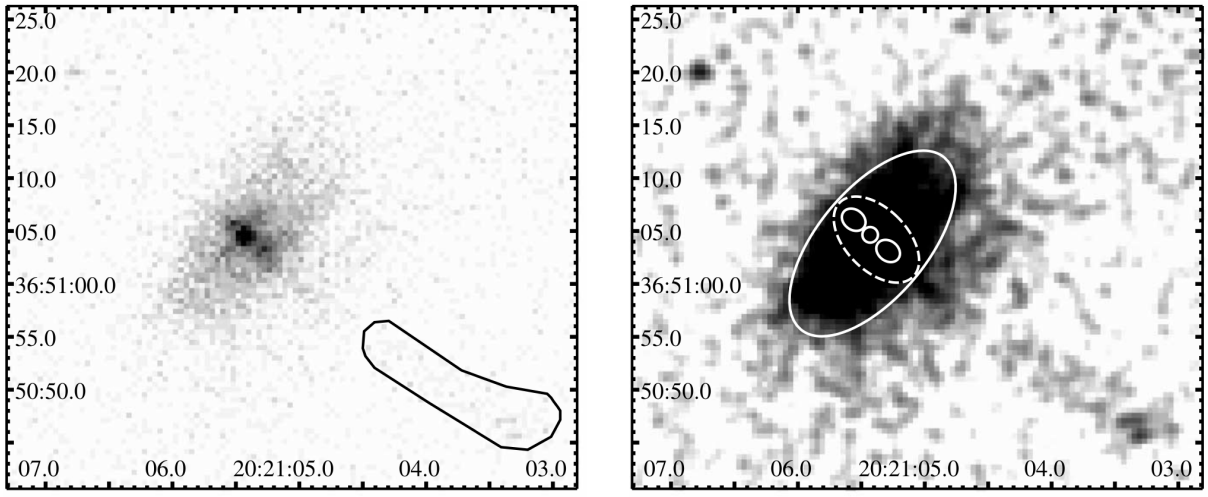

Figure 1.5: Image of the Dragonfly nebula in $1 - 7\,\mathrm{keV}$ from deep Chandra observations (Van Etten et al., 2008). Left: a soft stretch shows the double 'ridge' structure and the extraction aperture of the outer jet. Right: a deeper stretch and 1" Gaussian smoothing show the jets and diffuse emission. The extraction apertures for the pulsar, inner jets, and equatorial nebula.

TeV emissions from the PWN system

Some TeV sources are associated with the Dragonfly nebula and PSR J2021+3651. The study by Aliu et al. (2014) suggested that the system is a likely contributor to the VERITAS source VER J2019+368. This was confirmed by Mizuno et al. (2017) through X-ray studies of Suzaku and XMM-Newton data. They further found that a model of synchrotron radiation and inverse Compton scattering could explain most of the TeV emission of VER J2019+368. In addition, the TeV source HAWC J2019+368, 0.3° away from the VERITAS source, was also associated with the Dragonfly system (Albert et al., 2021), and was proposed to be the pulsar birth site (Mizuno et al., 2017). Through the spectral modeling with HAWC and Suzaku data, the true age of the Dragonfly pulsar was estimated as $\sim 7\,\mathrm{kyr}$ (Albert et al., 2021).

1.3.2 The Geminga pulsar

The Geminga pulsar (PSR J0633+1746) is a radio quiet, middle-aged pulsar, with a rotation period of $P = 0.237\,\mathrm{s}$ and a spin-down rate $\dot{P} = 1.1 \times 10^{-14}$. This corresponds to a characteristic age $\tau_c \simeq 3.4 \times 10^5\,\mathrm{yr}$, a surface dipole magnetic field $B_s \simeq 1.63 \times 10^8\,\mathrm{G}$ and a spin-down luminosity $\dot{E}_r \simeq 3.25 \times 10^{34}\,\mathrm{erg\,s^{-1}}$.

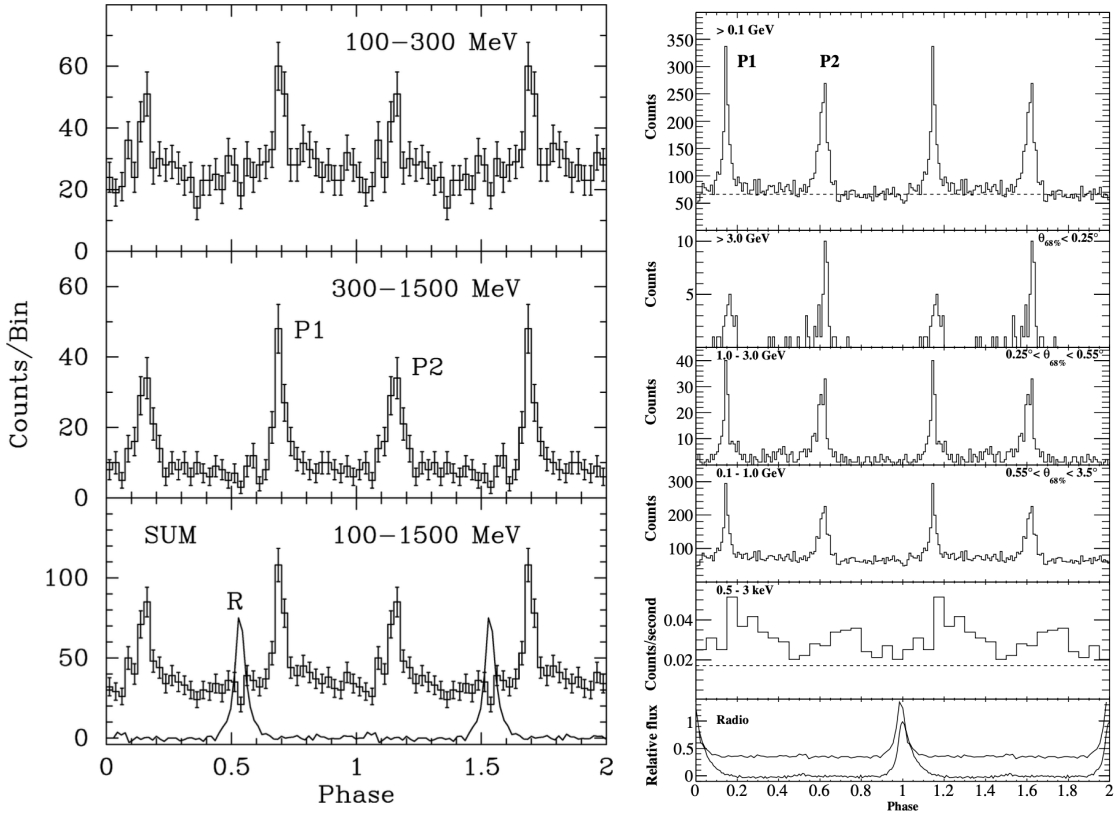

Figure 1.6: Phaseograms of the Dragonfly pulsar in the gamma-ray band. Left: AGILE observations in the 100-1500 MeV energy range (Halpern et al., 2008). Right: Top four frames: *Fermi*-LAT observations from 0.1 GeV to more than 3 GeV. Second frame from bottom: Chandra X-ray phaseogram. Bottom frame: the 1950 MHz radio profile from the GBT. (From Abdo et al. 2009)

Discovery of the Geminga pulsar

First detected by the SAS-2 and COS-B satellites (Fichtel et al., 1975; Bennett et al., 1977; Hermsen et al., 1977), the nature of the gamma-ray source Geminga (2CG 195+04) remained unknown for decades. Its potential X-ray counterpart, 1E 0630+178, was found within the COS-B error box by the Einstein Observatory (Bignami et al., 1983). The decisive identification came from the X-ray observations with ROSAT satellite (Halpern and Holt, 1992). Pulsations with a period of $P \simeq 0.237\,\mathrm{s}$ were detected, which confirmed that Geminga is a pulsar. Subsequently, the gamma-ray pulsations were also discovered in the data from EGRET observations (Bertsch et al., 1992), as well as in the archival COS-B (Bignami and Caraveo, 1992) and SAS-2 data (Mattox et al., 1992), further supporting the identification of the Geminga pulsar.

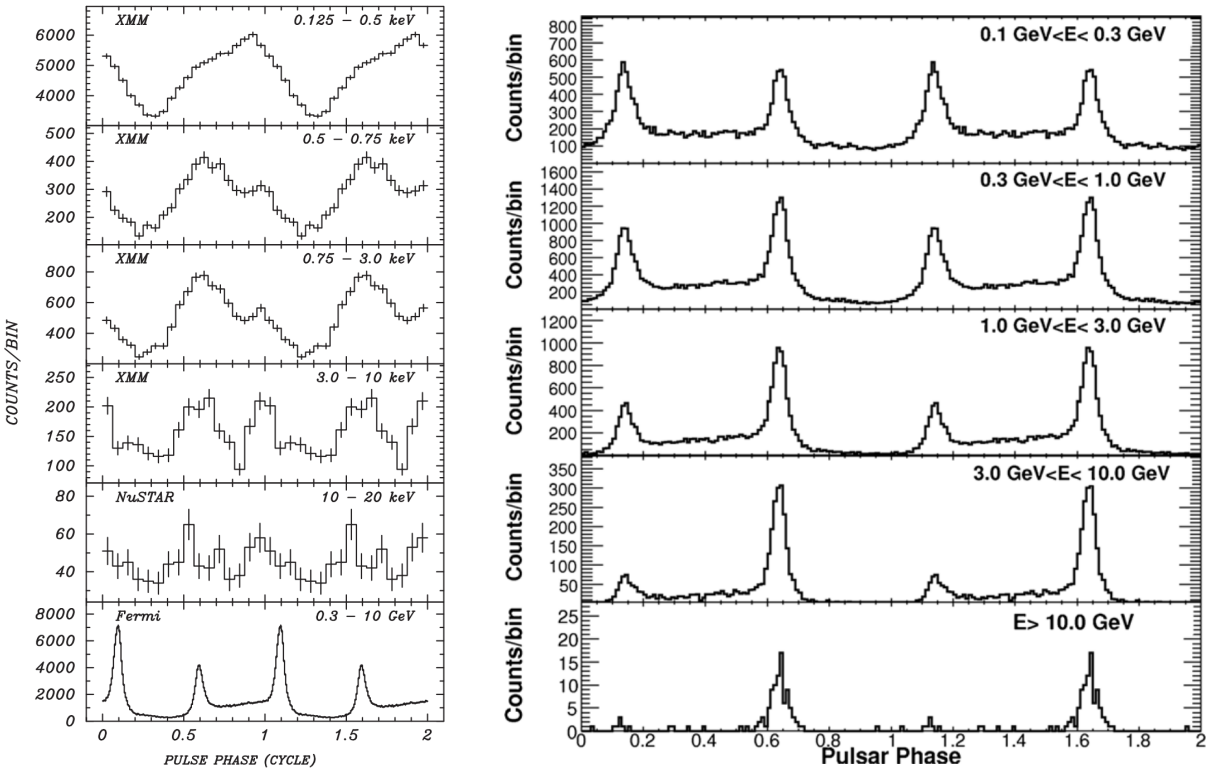

Figure 1.7: Phaseograms of the Geminga pulsar in the X-ray band (left, XMM-Newton and NuSTAR observations, Mori et al. 2014) and the gamma-ray band (right, *Fermi*-LAT observations Abdo et al. 2010d)

.

X-rays observations

The X-ray spectrum of Geminga consists of two components: a) the synchrotron radiation in the magnetosphere, which dominates at $E \gtrsim 0.7\,\mathrm{keV}$ and can be described by a power-law with index $\Gamma \simeq 1.7$ (Jackson et al., 2002). b) the thermal emission, which can not be modeled by a single blackbody component(Mori et al., 2014), and may contain contributions from hot spots on the pulsar surface (Caraveo et al., 2004). Fig. 1.7 shows the X-ray phaseograms of Geminga obtained with XMM-Newton and NuSTAR observations (Mori et al., 2014). It is very different from the gamma-ray ones, indicating different radiation processes in the two energy bands.

Gamma-ray emissions

The pulsed gamma-ray emissions were first detected by EGRET at energies above 300 MeV, and two peaks separated by a phase difference of $\Delta\phi \simeq 0.5$ were found. (Bertsch et al.,

1992). Early analysis of the EGRET observations found a power-law spectrum with $\Gamma \simeq 1.5$ between 30 MeV to 2 GeV (Mayer-Hasselwander et al., 1994). A high-energy spectral turnover around a few GeV was later revealed in the phase-resolved study with EGRET data (Fierro et al., 1998). For the spectra of individual components, the P2 component showed a much flatter spectrum than others, which was also the hardest spectrum ever measured by EGRET.

The average spectrum of Geminga from the first year *Fermi*-LAT observations was described by a power law with exponential cutoff, with photon index $\Gamma \simeq 1.3$ and cutoff energy $E_0 \simeq 2.46\,\mathrm{GeV}$ (Abdo et al., 2010d). Freeing the exponential index b provided a better fit to the Fermi data, and yielded a value of $b = 0.81$. The preference for a sub-exponential cutoff was confirmed in the second *Fermi*–LAT pulsar catalog (Abdo et al., 2013). Abdo et al. (2010d) also found a decrease of P1/P2 ratio with increasing energy. As is shown in Fig. 1.7, the P1 component became almost undetectable at energies above 10 GeV. From Fermi observations, the spectral features supported outer magnetospheric emission scenario.

Early IACT observations by VERITAS (Aliu et al., 2015) and MAGIC (Ahnen et al., 2016) did not detect significant gamma-ray emissions from the Geminga pulsar. In 2020, the pulsed gamma-ray emission in the $15\,\mathrm{GeV} - 75\,\mathrm{GeV}$ energy range was first revealed by MAGIC observations (MAGIC Collaboration, 2020), after employing the special, low-energy Sum-Trigger-II system (Dazzi et al., 2021). The MAGIC observations ruled out the pure exponentially cutoff power-law model for the P2 component. Furthermore, a simple power-law model was favored over the sub-exponential cut-off, indicating the presence of an inverse Compton component.

This thesis is structured as follows. Chapter 2 presents the analysis of the MAGIC archival observations of the Dragonfly pulsar, and investigates the pulsed gamma-ray emission in the $30\,\mathrm{GeV} - 200\,\mathrm{GeV}$ energy range. Chapter 3 studies the spectrum of the pulsed emission from the Geminga pulsar with `Gammapy` analysis. An MCMC technique with Tikhonov regularization is implemented for flux point estimation. The results are summarized and discussed in Chapter 4.

Chapter 2

Searching for the Pulsed Gamma-ray Emission from the Dragonfly Pulsar

The Dragonfly pulsar (PSR J2021+3651) is an intermediate-aged pulsar, with a spin period of $P = 103.7$ ms. Gamma-ray pulsations from this source were first revealed by AGILE in 2008 (Halpern et al., 2008), with two pulsed components detected in the $100 - 1500$ MeV energy range. The pulsed gamma-rays were also detected with the *Fermi* Large Area Telescope (LAT) from 0.1 GeV to more than 3 GeV energy, whose spectrum can be well-described by a power law with an exponentially cut-off (Abdo et al., 2009). With ground-based Imaging Atmospheric Cherenkov Telescopes (IACTs), while the TeV emission of its pulsar wind nebula has been studied (e.g., Aliu et al. 2014), its very-high-energy (VHE) pulsations remains unexplored, which is important to understand the gamma-ray emission mechanism in pulsar magnetosphere.

To search for the pulsations of the Dragonfly pulsar between 30 GeV to 200 GeV, we analyzed the MAGIC archival observations from 2014 with MARS, the MAGIC Standard Analysis Software (Zanin et al., 2013), and applied specialized, non-standard procedures required by the low-energy pulsar data analysis.

This chapter is structured as follows. Sec. 2.1 provides an overview of the MAGIC data on the Dragonfly pulsar. The data analysis process and underlying theories are discussed in Sec. 2.2. The pipeline begins at the raw, binary format data produced by the telescopes and ends with a list of events with estimated physical quantities and pulsar phase. The pulsar phaseogram is produced in Sec. 2.3, and the detection significance of pulsed signal is evaluated. A work summary and a discussion on the results are presented in Sec. 2.4.

2.1 Data overview

The MAGIC observations on the Dragonfly pulsar were conducted between July and August in 2014. After quality selection, data from 110 runs were collected in 17 nights of observations, with a total effective time of approximately 40 hours.

The observations were taken in the wobble mode, in which the telescopes were pointed to positions around the source with an offset of 0.4 degrees. Two wobble positions were adopted in Dragonfly observations: the wobble angle of $\omega = 35°$ and its opposite position $\omega = 215°$. The wobble observation strategy allows one to estimate the background without conducting dedicated observations (Fomin et al., 1994). In standard observations, the background can be estimated either from different positions in the camera simultaneously, or at the same camera position as the source but at a different time. For pulsars, the background is determined based on phase, which enables a simultaneous background estimation at the same position (see Sec. 2.3.1). In practice, however, pulsar observations are also taken in wobble mode, in order to study the surrounding extended emission, such as the emission from the pulsar wind nebula.

2.2 Data reduction

An overview of the analysis workflow is illustrated in Fig. 2.1. The pipeline aims to produce full-analyzed events with estimated energy, particle type, incoming direction and pulsar phase. This chapter presents the analysis work on the Dragonfly data, and briefly introduces the relevant theories based on Ceribella (2021). The technical details are presented in Appendix A. I refer interested readers to Ceribella (2021) for more detailed descriptions.

2.2.1 Raw data processing

The main goal of raw data processing is to obtain the charge and arrival time distribution in the camera images for the extracted Cherenkov events. This process relies on the pedestal and calibration files taken in special data runs.

The signal extraction, calibration and special image cleaning for low-energy analysis were performed using software `Sorcerer`. It was first executed in C-mode, which processed the pedestal and calibration files to estimate the background level and compute basic calibration factors. Then it ran in Y-mode, which actually performed calibration to all data files with C-mode outputs, frequently updating the values using interleaved pedestal and calibration events. The theories and methods behind the raw data processing are discussed below.

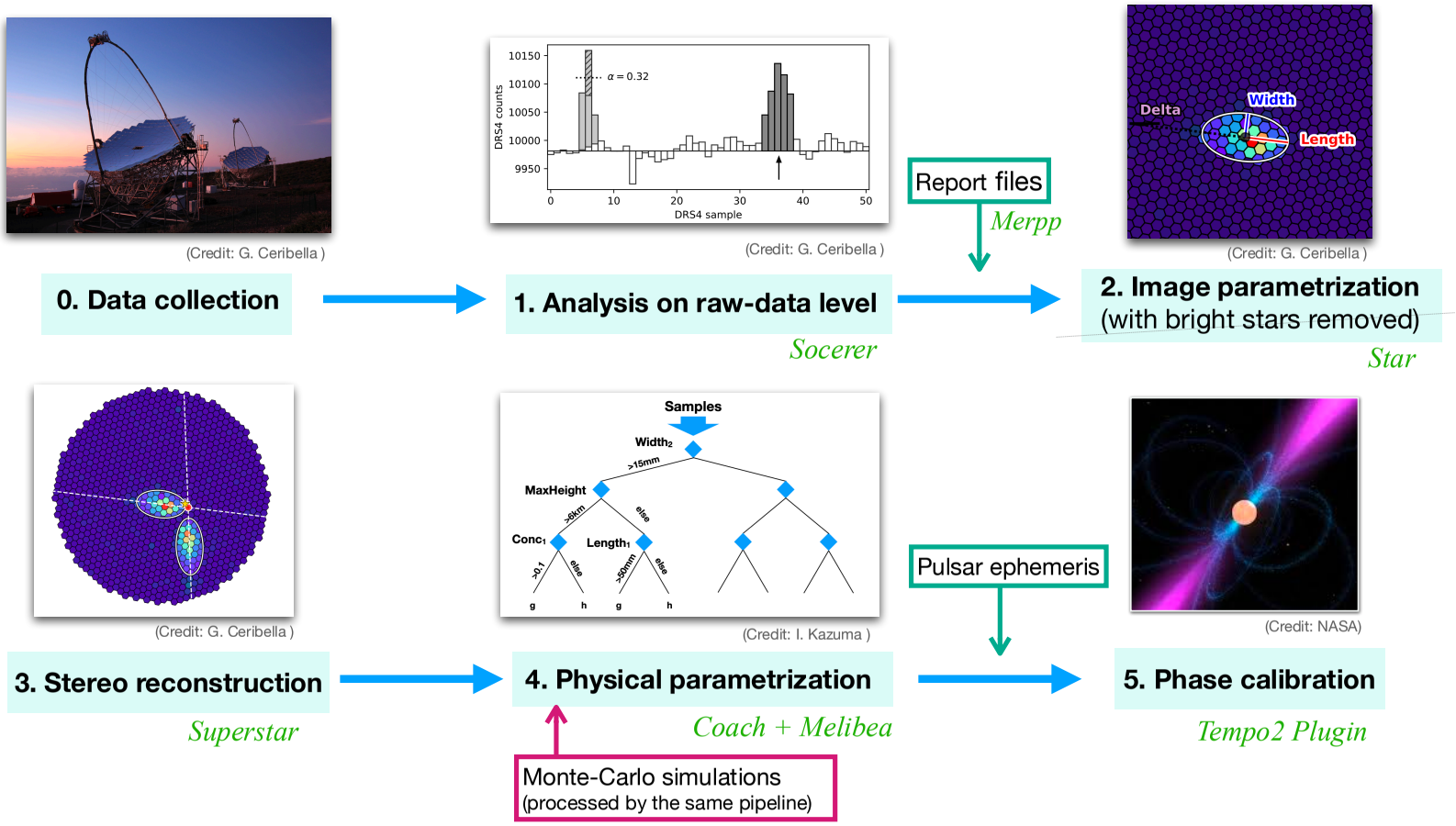

Figure 2.1: An overview of the analysis workflow. It starts with raw-data level analysis (Sec. 2.2.1), including signal extraction, calibration and image cleaning, in which special spike removal and image cleaning algorithms are employed to improve the low-energy performance. After that, image and stereo parameters are estimated (Sec. 2.2.2). The physical parameters are reconstructed using random forest estimators trained on Monte-Carlo simulations and off observations (Sec. 2.2.3). Pulsar phase information is finally added based on the pulsar rotation model (Sec. 2.2.4). The relevant MAGIC software is shown in green.

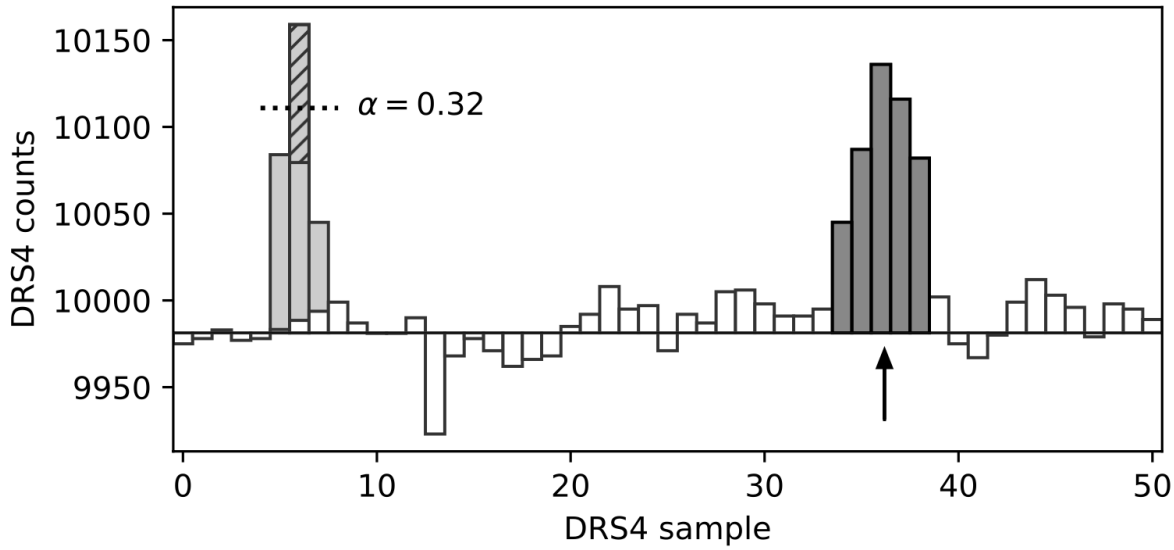

Figure 2.2: An example of the PMT waveform in a pixel for a triggered event, from Ceribella (2021). The genuine Cherenkov signal is shown in the right dark shaded area. The pulse on the left is a spike. The spikeness α measures the extent to which the local maximum exceeds the average value of its neighbors. Pulses with spikeness larger than the pre-defined threshold are removed. The x-axis is the DRS4 sample in unit of local UTC time, and the y-axis is the readout counts. These units need to be calibrated into more physically meaningful quantities.

Raw data

The raw data consists of the PMT waveforms for all pixels for every triggered events. During the data-taking process, electric signals are sent to the trigger system and the sampling electronics. When a trigger occurs, 50 samples are digitized by the Domino Ring Sampler v.4 (DRS4) chips and stored for every pixel. A typical waveform is shown in Fig. 2.2. It records the readout counts for the time slices around the trigger time in a pixel. The duration of one time slice is roughly $1/1.64\,\mathrm{GHz} = 0.6\,\mathrm{ns}$. The horizontal baseline reflects the background level and needs to be subtracted from the waveform for each pixel. It is estimated from pedestal events as the mean value of readout counts.

Signal extraction

In `Sorcerer`, the sliding window method is applied to extract the signal from a waveform. With a fixed size matching the duration of a typical Cherenkov signal, the sliding window searches for the position that gives the largest integrated counts within it. From the sliding window extractor, the total readout counts, or the charge C_i of the signal in the i-th pixel

is obtained, and the signal arrival time is the count-weighted average of the corresponding time slices.

In a waveform, noise features can be produced by the readout system and might be misidentified as a signal. These artifacts include pseudo-pulses, which are predictable using the previous event, and spikes, which are narrow pulses generated randomly (Fig. 2.2). Spike removal is crucial for analyzing the low-energy events below 100 GeV. Taking advantage of the property that spikes are narrower than the Cherenkov pulses, special algorithms have been developed to effectively remove spikes while preserving the true signals.

Calibration

After signal extraction, the charge and arrival time of a signal is given in arbitrary units of readout counts and time slices, which need to be calibrated to more physically meaningful quantities.

The time is calibrated to account for the differences in length of the optical fibers. A more accurate calibration on the time difference between pixels is described in Aleksić et al. (2016).

For the readout count, we need to convert it into the equivalent photo-electrons (PhE) count, a more physical unit representing the total deposited charge. The F-factor method (Mirzoyan, 1997) is employed to compute the conversion factor using the pedestal and calibration files.

The principle of this method can be understood through the following derivation. For a signal in pixel i with Q_i PhE counts, assuming a conversion factor k_i, the mean readout count is given by $C_i = k_i Q_i$. If we further assume Poisson statistics for this signal, its standard deviation will be $\sigma_{C_i} = \sqrt{Q_i}/C_i$. By eliminating the unknown Q_i, we can obtain the conversion factor $k_i = \frac{C_i}{\sigma^2_{C_i}}$.

In reality, the conversion factor is computed from the the mean $C_{\mathrm{cal},i}$ and its standard deviation $\sigma_{\mathrm{cal},i}$ of the calibration events. In addition, we need to consider a correction for the non-Poissonian response of PMTs, described by the F-factor, as well as the background fluctuations $\sigma_{\mathrm{ped,i}}$. The conversion factor then becomes

$$k_i = F^2 \frac{C_{\mathrm{cal},i}}{\sigma^2_{\mathrm{cal},i} - \sigma^2_{\mathrm{ped,i}}} \ . \tag{2.1}$$

A flat-field calibration is further needed to correct for the different response between pixels under uniform illumination. To ensure we have the same signal for the same light intensity, the conversion factor for the *equivalent* PhE is determined as

$$k'_i = \frac{\bar{Q}}{C_{\mathrm{cal},i}} = \frac{1}{C_{\mathrm{cal},i}} \frac{\sum_j k_j C_{\mathrm{cal},j}}{N} \ . \tag{2.2}$$

Typically, one equivalent PhE corresponds to about 60 readout counts.

As the sky background and the PMT response may vary in an observational run, interleaved pedestal and calibration events are recorded during data taking. In calibration, the conversion factor for each pixel is frequently updated using these events, with a typical interval of 40 s.

Image cleaning

In standard data reduction pipeline, the purpose of image cleaning is to identify the relevant pixels for the extracted Cherenkov signals. However, for low-energy pulsar analysis, to further reduce the energy threshold, the MaTaJu cleaning method is applied. It performs analysis based on the PMT waveforms, rather than the calibrated camera images. Basically, it identifies the core and rings of boundary pixels iteratively, according to given charge thresholds and narrow time windows, which helps to distinguish the dim events from the background. Interested readers can refer to Shayduk and Consortium (2013) for more details.

2.2.2 Image parameterization and stereo reconstruction

From the charge and arrival time distribution obtained in the previous steps, we can compute several key parameters that describe the properties of shower images of Cherenkov events. These image parameters are the basis for estimating the physical properties of the incident particles.

The MAGIC software `Star` was used to perform image parameterization. To reduce the impact of the light from surrounding bright stars on parameter estimation, we identified and removed several stars near the Dragonfly pulsar in the field of view. This is a non-standard approach required for low-energy analysis. Based on some image parameters, the three-dimensional (3D) geometry of the shower can be reconstructed using `Superstar` from stereo observations from two MAGIC telescopes.

Image parameters

The image parameters are defined based on the moments of the charge distribution, as well as the time development of the shower. These parameters, also referred to as the Hillas parameters, were first proposed in Hillas (1985), with a motivation of distinguishing gamma-ray showers from background hadronic showers based on their width, length and orientation.

For a clear understanding, the mathematical definitions of the main image parameters are

provided below:

- Size: the total equivalent photo-electrons in the shower image. It is approximately proportional to the energy of the primary particle for a fixed incident direction.

$$\text{size} = \Sigma_i q_i \ . \tag{2.3}$$

- Position: the first moments of charge distribution, defined as charge-weighted average of the camera pixel positions.

$$(\bar{x}, \bar{y}) = \frac{1}{\text{size}} \sum_i (x_i, y_i) \cdot q_i \ . \tag{2.4}$$

- Length, width and the projected shower direction: calculated from the covariance matrix that is derived from the second moments of charge distribution:

$$\begin{aligned} \sigma_x^2 &= \frac{1}{\text{size}} \sum_i (x_i - \bar{x})^2 \cdot q_i \\ \sigma_{xy} &= \frac{1}{\text{size}} \sum_i (x_i - \bar{x})(y_i - \bar{y}) \cdot q_i \\ \sigma_y^2 &= \frac{1}{\text{size}} \sum_i (y_i - \bar{y})^2 \cdot q_i \ . \end{aligned} \tag{2.5}$$

  The length and width parameters are given by the square root of the eigenvalues of the covariance matrix, corresponding to the half-lengths of the major and minor axis of the shower ellipse, respectively. They are important for distinguishing primary particle types. For example, images of hadron induced showers are generally wider than the gamma-ray induced ones. The projected shower direction, defined as the angle between the major eigenvector and the camera x-axis, is essential for the stereoscopic shower reconstruction.

- Time gradient: contains information on the time development along the major axis of the shower ellipse.

Bright star removal

The presence of a distant noise source in the shower image, such as the light from a bright star near the target, can introduce large uncertainties in the computation of the second moments, as it is sensitive to pixels far from the shower position. The resulting inaccurate Hillas parameters will further lead to unreliable estimation on physical quantities. Compared to the standard procedure, the impact of bright stars is more severe in low-energy analysis, in which the events are dim and contaminated by large background noise.

To reduce the influence of starlight on image parameter calculation, we identified and removed the bright stars near the Dragonfly pulsar. Table 2.1 lists the bright stars in the MAGIC field of view centered on the Dragonfly pulsar, which were identified in SIMBAD[1] as stars with a visual magnitude m_V less than 6. For each bright star, a circular region with a radius of 50 mm was cut in the image. The relevant pixels will be masked in the following analysis.

Source Name	RA (h)	Dec (°)	m_V
b03 Cyg	20.242	36.806	4.99
35 Cyg	20.365	34.983	5.16
HD 194335	20.396	37.476	5.90
P Cyg	20.296	38.033	4.82
36 Cyg	20.308	37.000	5.58
42 Cyg	20.489	36.455	5.90

Table 2.1: Bright stars ($m_V < 6$) in the MAGIC field of view centered on the Dragonfly pulsar. A cut with a radius of 50 mm was applied to remove these stars from analysis.

Stereo reconstruction

The goal of stereo reconstruction is to construct the 3D geometry of the shower from the camera images of both MAGIC telescopes. As the two MAGIC telescopes observe the air shower from different angles, their images contain complementary information on the 3D properties of the air shower. The stereo reconstruction was performed using the software `Superstar`, based on the data previously analyzed by `Star` from the two telescopes.

The main properties estimated in this step includes:

- The direction of the primary particle: the key physical parameter we focus on, which in principle can be computed as the intersection of the major axes of the two images. The estimation accuracy can be improved with the machine learning-based DISP method (see Sec. 2.2.3);
- DISP: the distance between the shower core and the projected incoming direction;
- Theta square θ^2: the angular distance between the source and the direction of the primary particle, which is important for event selection in Sec. 2.3.2;
- The impact parameter: the distance between the shower axis and the telescope position;

[1] `https://simbad.u-strasbg.fr/simbad/sim-fbasic`

- Shower maximum height: the altitude at which the shower reaches its maximum particle density.

2.2.3 Physical parameter estimation

Physical properties of the events, including the type, energy and the incoming direction of the primary particles, are essential for higher-level scientific products, such as the light curve and energy spectra.

Physical parameter estimation relies on Monte-Carlo (MC) simulations. This is because the Earth's atmosphere, as the 'detector' of ground-based Cherenkov telescopes, cannot be calibrated directly. The complex processes involved are simulated in MC simulations, including particle interactions and shower development (Heck et al., 1998), Cherenkov light propagation (Sobczynska, 2002), and the instrument response (Moralejo, 2003; Blanch and Moralejo, 2004). By processing these MC files in the same analysis pipeline, image parameter distributions for primary particles with different known properties can be obtained. This enables us to train random forest (RF) estimators, which are classification systems with a large number of decision trees constructed from a set of discriminating image parameters, and estimate the type, energy and direction of the primary particles for observed events. Interested readers can refer to Ishio (2020) for further information on the RF method in MAGIC.

For physical parameterization, we produced relevant random forests estimators with the MAGIC software `Coach`. The models were trained using MC simulations different from the standard ones. These RF estimators were applied to the observational data using the software `Melibea`, and the resulting estimated physical properties are discussed below.

Tailored Monte-Carlo simulations and random forest estimators

In the Dragonfly pulsar analysis, two types of training samples were used in `Coach` to construct random forest estimators: a) hadron events from the observations of the Geminga pulsar, which contain mostly cosmic rays due to the low gamma-ray emission of the source; b) gamma-ray events from Monte-Carlo simulations tailored for pulsar analysis.

The tailored Monte-Carlo simulations contain a larger number of low-energy events, approximately two orders of magnitude larger than that in the standard MC sets, in order to reduce uncertainties in parameter estimation caused by the insufficient MC events in the $E_{\rm true} < 50\,\mathrm{GeV}$ energy range. In addition, the telescope pointing was adjusted to match the trajectory of the source, and the effect of removing bright stars was also considered. For more details on the tailored Monte-Carlo simulations, interested reader can refer to Sec. 4.10 in Ceribella (2021).

In this work, since no MC files tailored for the Dragonfly pulsar are currently available, we

File	θ [deg]	E [GeV]	Event density	Event Number	Purpose
17	$5-30$	$5-500$	2^{14}	1.83×10^7	RF training
19	$5-30$	$500-5000$	1652	1.84×10^6	RF training
15	$5-30$	$5-500$	2^{16}	4.17×10^7	Event selection
18	$5-30$	$5-500$	2^{16}	3.14×10^7	Event selection
20	$5-30$	$500-5000$	3305	3.69×10^6	Event selection

Table 2.2: The tailored Monte-Carlo simulations in the Dragonfly pulsar analysis used for two purposes: a) training random forest estimators; b) event selection and energy migration matrix calculation. They were originally produced for the Crab pulsar in the work of Ceribella (2021).

used the MC simulations originally produced for the Crab pulsar in the work of Ceribella (2021) to train the random forests, whose properties are listed in Table 2.2. If significant pulsations are detected, special MC simulations for the Dragonfly pulsar can be produced accordingly.

Hadronness

To distinguish gamma-rays from hadronic events, the hadronness h is introduced to represent the probability that an event has a hadronic origin. A value of $h = 1$ corresponds to a hadron-induced event, while $h = 0$ indicates a gamma-induced one. This parameter is important for separating gamma-rays from the large cosmic-ray background, and energy-dependent hadronness cuts are typically applied in event selection (see Sec. 2.3.2).

The hadronness of each event was estimated by applying the gamma/hadron separation RF to observations with `Melibea`. In this process, each event went through all decision trees, obtaining a classification of 0 or 1 from each tree, and the final hadronness value is the average of results from all decision trees.

The hadronness distributions for gamma-rays and hadrons vary with energy. At low energies, it is difficult to distinguish the two distributions, because their image parameters are intrinsically less distinctive in this energy range. In our low energy analysis, more conservative cuts are considered in event selection.

Stereo DISP

The DISP method was employed to improve the direction reconstruction of the primary particles (Saito and Sitarek, 2009). The method mentioned in the previous section can have large uncertainties in the estimated direction, if the two image axes are relatively parallel.

The DISP parameter was estimated for individual telescopes by the stereo DISP RF estimators, which were trained using simulated gamma-rays. The final DISP for each event is

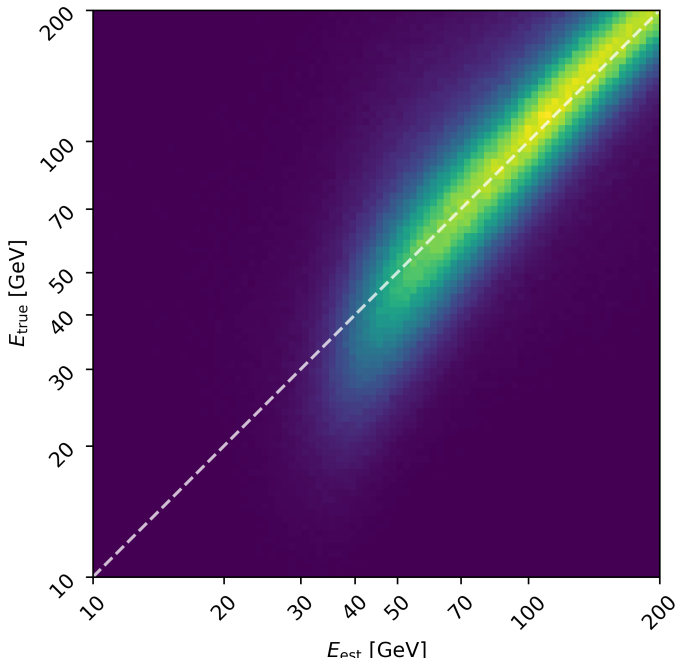

Figure 2.3: The energy migration matrix for the random forest estimator in this analysis. It shows the energy resolution in different energy range.

the average of the results from two telescopes.

Energy estimation and the migration matrix

The energy of the primary gamma-ray is roughly proportional to the number of Cherenkov photons in the air shower. However, the amount of received light also depends on other factors, such as the viewing geometry and the incoming direction. The traditional method for energy estimation is through look-up tables (LUTs). This method divides the simulated gamma-ray events in bins of various parameters and assigns the mean energy of the samples to each bin. The energy reconstruction is improved by the new RF estimator method (Ishio, 2020), which is employed in this analysis.

To evaluate the performance of the energy estimator, the energy migration matrix was produced using Monte-Carlo sets different from those for RF training (see Table 2.2). The migration matrix quantifies the probability of an event with true energy $E_{\rm true}$ being reconstructed with energy $E_{\rm rec}$. Fig. 2.3 shows the migration matrix for the energy RF estimator, whose x axis is the estimated energy, and y axis is the true energy in simulated MC events. At $E_{\rm true} > 50\,{\rm GeV}$, the spread of the reconstructed energies for a given true energy is small, indicating a good energy resolution. However, at $E_{\rm true} < 50\,{\rm GeV}$, events at a given $E_{\rm true}$ are migrated to larger reconstructed energies, meaning that the energy

estimation is biased. This is because the low-energy events that show similar characteristics as the high energy ones have a higher probability to be detected.

2.2.4 Pulsar phase

The pulsar phase for each event were added in the fully-analyzed files using the `Tempo2 Plugin`. As pulsars are characterized by periodical rotations, selecting events based on their phases allows us to efficiently reduce the background noise and detect gamma-ray pulsations.

To assign phase to each event, the pulsar ephemeris, a model for pulsar rotation, is required. The ephemeris provides the rotation frequency and its time derivatives $(\nu_0, \dot{\nu_0}, \ddot{\nu_0})$ at the reference epoch t_0. The pulsar rotation frequency at time t can then be predicted using the Taylor expansion:

$$\nu(t) = \nu_0 + \dot{\nu_0}(t - t_0) + \ddot{\nu_o}(t - t_0)^2 + ... \ , \tag{2.6}$$

where the decrease of pulsar spin is a result of energy loss. Finally, we can obtain the pulsar phase by integrating the rotation frequency over time.

For the Dragonfly pulsar, we adopted pulsar ephemeris provided in the third *Fermi*-LAT catalog of gamma-ray pulsars[2](Smith et al., 2023), which covers the time span between MJD 54683 (5. August 2008) and MJD 59062 (1. August 2020). We further employed the updated version of MAGIC `TEMPO2 plugin` (see Sec. 4.6.1 in Ceribella 2021), to translate the event arrival time to the barycentric time in the solar system and compute pulsar phase. In the time calibration, several timing delay effects were corrected (for a review see Backer and Hellings 1986) to obtain a correct phaseogram.

2.3 Phaseogram of the Dragonfly pulsar

To search for the gamma-ray pulsations in the estimated energy range of 30 GeV to 200 GeV, the phaseogram of the Dragonfly pulsar was produced, which is a histogram of event counts binned by phase. The signal and background regions were determined from *Fermi*-LAT observations and blindly applied to the MAGIC data, as discussed in Sec. 2.3.1. To further suppress the cosmic-ray background, events were selected by applying cuts on hadronness and θ^2, whose criteria are presented in Sec. 2.3.2. Finally, the results of phaseogram and detection significance are presented in Sec. 2.3.3.

[2] `https://fermi.gsfc.nasa.gov/ssc/data/access/lat/3rd_PSR_catalog/3PC_HTML/3PC_TimingModels/J2021+3651_LAT_JBOTZR.par`

Region	μ	σ_L	σ_R	Phase Range	Size
P1	0.120 ± 0.004	0.01 ± 0.004	0.020 ± 0.004	$0.090 - 0.159$	0.069
P2	0.596 ± 0.004	0.032 ± 0.004	0.013 ± 0.003	$0.533 - 0.622$	0.089
OFF	–	–	–	$0.660 - 1.045$	0.385

Table 2.3: Signal and background regions for the Dragonfly pulsar, determined from the *Fermi*-LAT phaseogram in the $1 - 30$ GeV range by fitting asymmetric Gaussian functions. The best-fit parameters and their errors are also listed.

2.3.1 Phase regions

The signal and background regions for pulsars are determined based on phase, which is an advantage of pulsar analysis. This approach enables a simultaneous estimation of the background at the same camera position as the signal, thus reducing the potential systematics due to the time differences and the inhomogeneities in camera efficiency. Furthermore, by folding the data over many rotation periods, the periodic signals, if present, become more significant, while the contribution of background noise that follows a Gaussian distribution is averaged out.

The signal and background regions of the Dragonfly pulsar were determined from *Fermi*–LAT observations, in order to provide an independent determination that is not biased by the results from MAGIC data. Theses regions, also referred to as the on and off regions, will be used in Sec. 2.3.3 to obtain the observed counts and calculate the detection significance.

Using the *Fermi*-LAT data from Aug. 2008 to Dec. 2019 (Abdollahi et al., 2020), we produced the phaseogram in the $1 - 30$ GeV energy range, which is adjacent to the energy band of MAGIC observations. As is shown in Fig. 2.4, the two significant pulsations P2 and P1 in this phaseogram were fitted separately with an asymmetric Gaussian function:

$$f(x, \mu, \sigma_L, \sigma_R) = \begin{cases} A_0 \exp\left(-\frac{(x-\mu)^2}{2\sigma_L^2}\right) , & \text{if } x < \mu \\ A_0 \exp\left(-\frac{(x-\mu)^2}{2\sigma_R^2}\right) , & \text{if } x \geq \mu \ . \end{cases} \tag{2.7}$$

The signal regions were determined as $\mu^{+2\sigma_R}_{-2\sigma_L}$, corresponding to 95% of the signal distribution. The background was selected as the region between P1 and P2, whose edges are 5σ away from the signal peaks. The best-fit parameters and phase intervals of on and off regions are listed in Table 2.3.

2.3.2 Event selection

To suppress the cosmic-ray background that dominates over the gamma-rays from the source, events were selected by applying energy-dependent cuts based on their hadronness and θ^2 values. Hadronness quantifies the probability for an event to have hadron origin, and

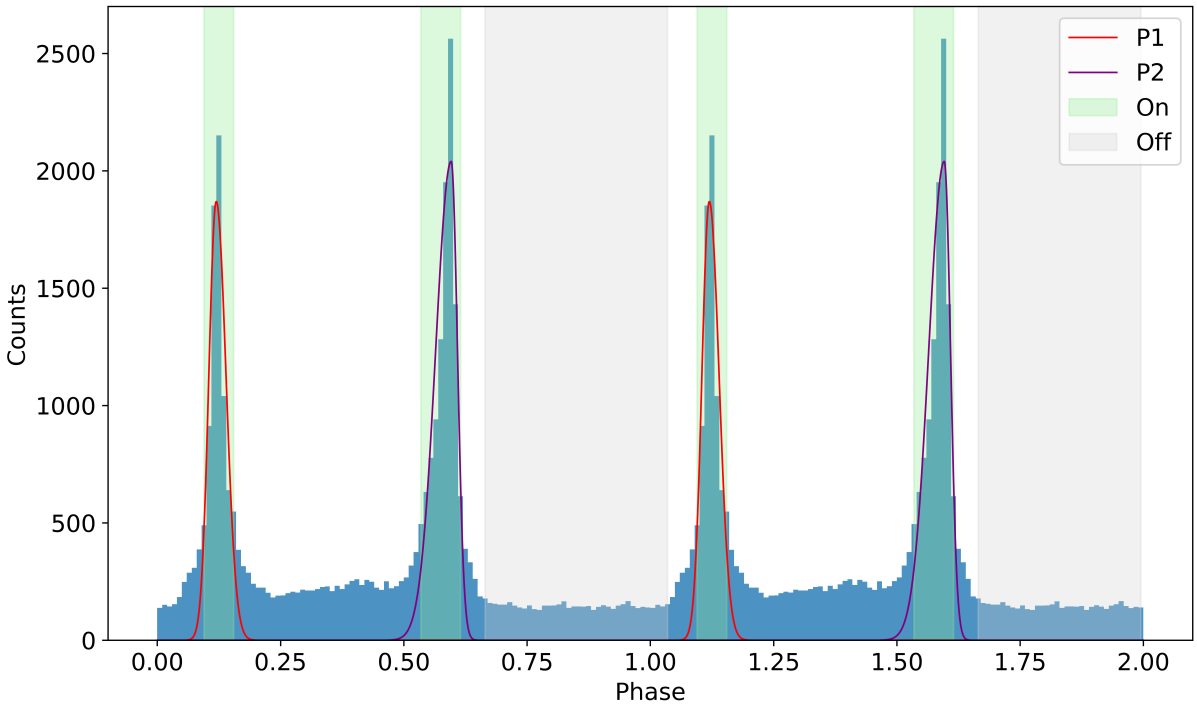

Figure 2.4: Phaseogram of the Dragonfly pulsar from *Fermi*-LAT observations in the $1 - 30\,\mathrm{GeV}$ energy range, which is adjacent to the MAGIC energy band. The pulsations P1 (red) and P2 (purple) are fitted with asymmetric Gaussian functions to determine the signal and background regions. The resulting on regions are highlighted in green and the off regions are shown in gray.

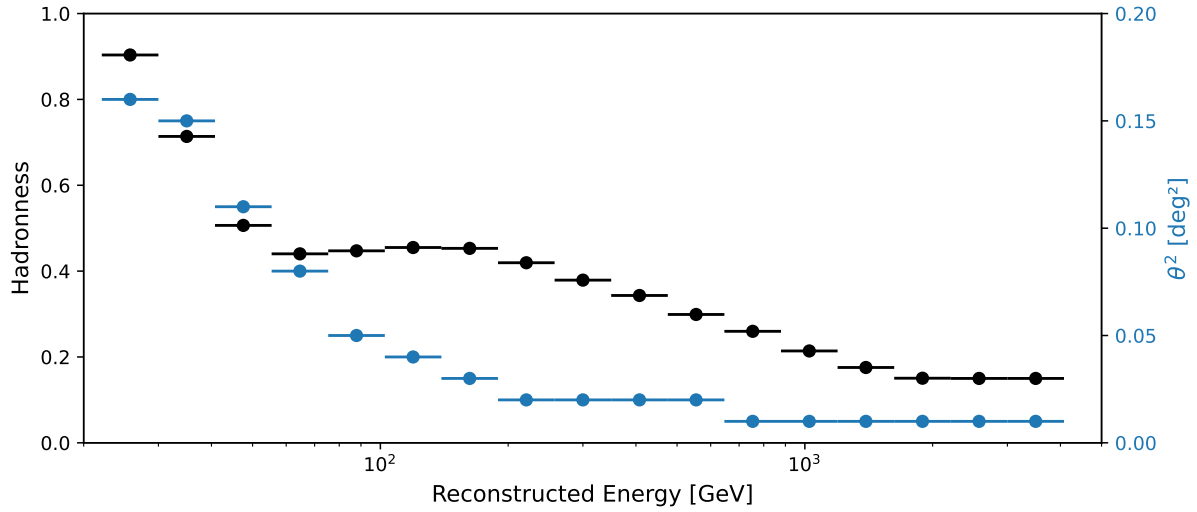

Figure 2.5: The energy-dependent hadronness (black) and θ^2 (blue) cuts used for producing the phaseogram of the Dragonfly pulsar, optimized for gamma-ray efficiencies of 90% and 75%.

θ^2 is the squared distance between the event and the source. Pulsed gamma-ray events are expected to be close to the pulsar position, as it is effectively point-like, while the isotropic cosmic-ray background has a flatter θ^2 distribution.

The cut condition is determined in terms of the gamma-ray efficiency parameter

$$\epsilon_\gamma = \frac{N^{\mathrm{MC}}_{\gamma,\ \mathrm{after\ cuts}}}{N^{\mathrm{MC}}_{\gamma,\ \mathrm{total}}} \ , \tag{2.8}$$

which is the percentage of the number of simulated gamma-ray events after the analysis cuts and the total gamma-ray events in the MC simulation. Smaller values of gamma-ray efficiency indicates better background suppression, but correspondingly, the probability of rejecting true gamma-ray events increases.

The gamma-ray efficiency $\epsilon_\gamma = 90\%$ was adopted for the hadronness cut, which means in every energy bin the probability for a real gamma ray event to be rejected is 0.1. For the θ^2 cut, the efficiency of $\epsilon_\gamma = 75\%$ was applied. The choice of these efficiency parameters follows other pulsar analysis in Ceribella (2021).

To obtain the cut values in each energy bin, the software `Flute` was run using MC simulations different from those for RF training, which are listed in Table 2.2. The resulting energy-dependent hadronness and θ^2 cuts, optimized for gamma-ray efficiencies of 90% and 75%, are shown in Fig. 2.5.

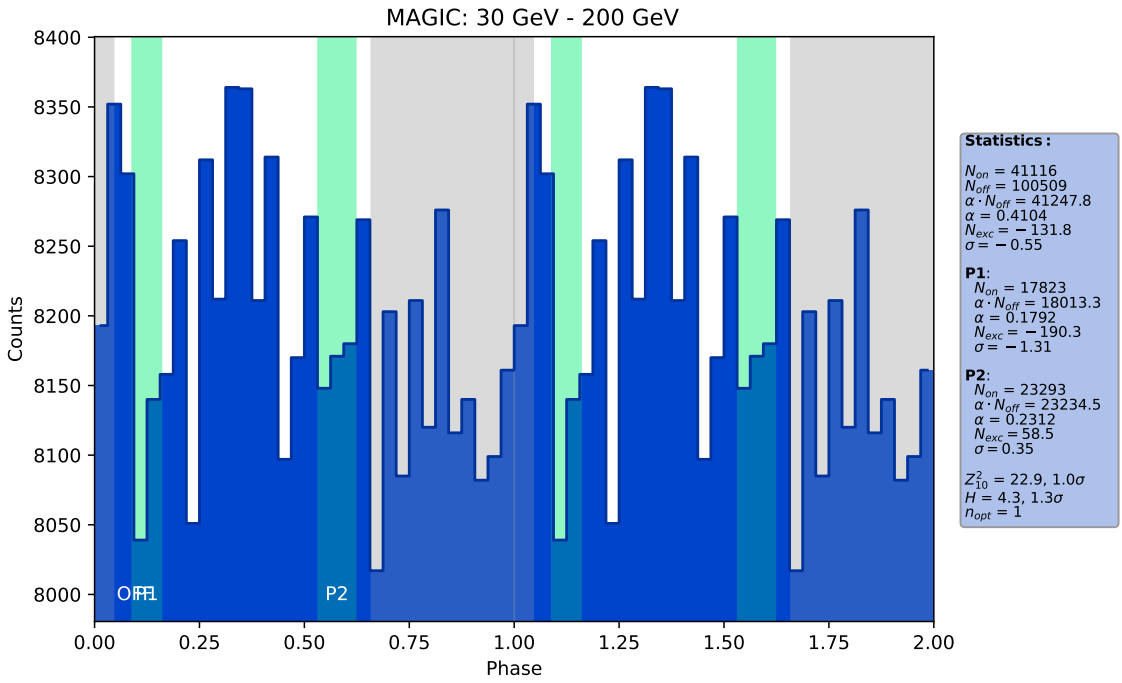

Figure 2.6: Phaseogram of the Dragonfly pulsar with MAGIC observations in the reconstructed energy range of 30 GeV to 200 GeV, which corresponds to the true energy range of $\sim$ 25 GeV to 200 GeV. The hadronness and θ^2 cuts optimized for gamma-ray efficiencies of 90% and 75% are applied. The signal (green) and background (gray) regions are determined *a priori* from *Fermi*-LAT data in the $1 - 30$ GeV estimated energy range. The phaseogram is dominated by background fluctuations, which is supported by non-significant results from the Li & Ma significance, Z^2_{10}, and H test. In conclusion, there is no significant detection for pulsed components in this energy range.

2.3.3 Phaseogram

Fig. 2.6 shows the phaseogram of the Dragonfly pulsar with approximately 40 hours of MAGIC observations in the reconstructed energy range of 30 GeV to 200 GeV, which corresponds to the true energy range of $\sim$ 25 GeV to 200 GeV. The hadronness and θ^2 cuts optimized for gamma-ray efficiencies of 90% and 75% were applied to increase the signal-to-noise ratio. The phaseogram is dominated by background fluctuations, and no significant pulsed emissions are detected.

The signal and background regions shown in this figure were determined *a priori* from *Fermi*-LAT data in the neighboring $1 - 30$ GeV estimated energy range, as described in Sec. 2.3.1. These regions were used to measure the on and off counts $N_{\rm on}$ and $N_{\rm off}$, which were then employed to quantify the detection significance.

Typically, the significance S is calculated using the Li and Ma (1983) formula:

$$S^2 = 2N_{\rm on} \log \left[\frac{1+\alpha}{\alpha} \cdot \frac{N_{\rm on}}{N_{\rm on}+N_{\rm off}} \right] + 2N_{\rm off} \log \left[(1+\alpha) \cdot \frac{N_{\rm off}}{N_{\rm on}+N_{\rm off}} \right] , \qquad (2.9)$$

where α is the ratio of exposures between on and off regions, here is the ratio of phase intervals. The significance quantifies the probability that the observed excess is produced by background fluctuations rather than astrophysical sources. In the phaseogram, a Li&Ma significance of -0.55σ was found, indicating that there is no pulsed emission.

Alternative statistical approaches were considered to determine the detection significance, which do not rely on the assumption of signal and background regions. In this work, two widely used methods in pulsar analysis, Z^2_{10} test (Buccheri et al., 1983) and H test (de Jager and Büsching, 2010), were applied to evaluate the deviation from a uniform phase distribution (no pulsations) in the periodic data. The resulting significance levels are at 1.0σ and 1.3σ, respectively. This confirms the conclusion that there are no significant pulsations in the MAGIC observations on the Dragonfly pulsar.

2.4 Summary and discussion

In this work, to search for the gamma-ray pulsations of the Dragonfly pulsar (J2021+3651) in the energy range from 30 GeV to 200 GeV, we performed data analysis for $\sim$ 40 h of MAGIC observations taken in 2014, and produced the pulsar phaseogram to detect the potential pulsed emissions.

The data reduction framework and the MARS software employed are summarized in Fig. 2.1. The technical details are provided in Appendix. A. As low-energy gamma-ray events are very faint, it is challenging to detect and distinguish them from the dominating background. Different sources of background and noise need to be carefully addressed:

a) Background light: pulsar observations were conducted in dark conditions, and bright stars in the field of view were all masked before the computation of image parameters.

b) Artifacts produced by the readout system: the spike removal algorithm was employed to prevent them from being identified as Cherenkov signal. Besides the artifacts, in the low-level analysis, MaTaJu cleaning was applied to effectively improve the low-energy performance and reduce the energy threshold.

c) Cosmic-ray background: tailored Monte-Carlo simulations with improved number of low-energy events were used to train the RF estimators. In addition, pulsar phases were added with high precision. Determining the background region based on phase allows for a simultaneous background estimation at the same camera position, which avoids several potential systematics. The statistical uncertainties in the background can also be reduced by folding events over rotation periods. Moreover, events were selected using hadronness

and θ^2 cuts, which further suppressed the cosmic-ray background and improved the signal to noise ratio.

The above procedures are different from the standard data reduction pipeline. They enable successful and robust analysis of low-energy gamma-ray events.

The final phaseogram and detection significance is shown in Fig. 2.6. It is dominated by random background fluctuations, and no significant pulsed emission is detected. This conclusion is further supported by the Z^2_{10} and H test, which obtains very low detection significances of 1.0σ and 1.3σ, respectively. The lack of significant detection could indicate that the Dragonfly pulsar inherently does not produce gamma-ray pulsations in the $30\,\mathrm{GeV} - 200\,\mathrm{GeV}$estimated energy range. However, VHE gamma-ray pulsations have been detected from the Vela (H.E.S.S. Collaboration, 2018), a pulsar with similar properties to the Dragonfly except for the distance. Considering that the Dragonfly is approximately more than 10 times farther away than the Vela, the non-detection could also be due to the limited observation time.

Chapter 3

Spectral Analysis of the Geminga Pulsar with Gammapy

The Geminga pulsar (PSR J0633+1746), a famous radio quiet pulsar with a rotation period of $P \simeq 0.237\,\mathrm{s}$, has a special place in the observations of gamma-ray pulsars. It is the third pulsar detected by the Imaging Atmospheric Cherenkov Telescopes (IACT), following the Crab (Aliu et al., 2008) and the Vela (H.E.S.S. Collaboration, 2018), and the first middle-aged pulsar to be detected. The MAGIC observations revealed its pulsed gamma-ray emission in the $15\,\mathrm{GeV} - 75\,\mathrm{GeV}$ energy range (MAGIC Collaboration, 2020), providing insights into the radiation process in the pulsar magnetosphere. The spectral analysis with the MAGIC Analysis and Reconstruction Software[1] showed a power-law spectrum with an index of $\Gamma = 5.62 \pm 0.54$, which is one of the steepest spectra ever measured by IACTs.

In this chapter, an analysis of MAGIC data of the Geminga pulsar with `Gammapy`[2] is presented. `Gammapy` is an open-source, community-driven Python package that allows multi-instrument analysis of gamma-ray data for various scenarios, including spectral, spectral-morphological, temporal, and survey analysis (Donath et al., 2023). As the official science tool for the Cherenkov Telescope Array Observatory (CTAO), its performance needs to be further tested. In this work, we focus on the 1D analysis of MAGIC pulsar data with `Gammapy`, improving the spectral analysis pipeline for data with low statistics and sources with steep spectra, and cross-checking our results with previous results from MARS.

In this work, we reanalyzed the MAGIC Geminga data using `Gammapy` and cross-checked the results with those from MARS. For the spectral point estimation process, we identified several issues with the `Gammapy` estimator and implemented a new technique to address them. It estimates the flux points using a stepped power-law model, with parameters estimated from Markov Chain Monte Carlo (MCMC) sampling with Tikhonov regulariation.

[1] MARS, (Zanin et al., 2013)

[2] `https://docs.gammapy.org/1.2/`

The structure of this chapter is as follows. A description of MAGIC observations on the Geminga pulsar and the corresponding low-level analysis is provided in Section 3.1. Section 3.2 describes the data reduction process for pulsar analysis in `Gammapy`, as well as the preparation of DL3 files. Section 3.3 presents the spectral parameter constraints using Poisson maximum likelihood fitting. Section 3.4 discusses the challenges of flux point estimation and introduces our new analysis pipeline based on the MCMC technique. The spectral analysis results of the Geminga pulsar and the performance of Gammapy analysis are summarized in Section 3.6.

3.1 MAGIC data

The MAGIC observations on the Geminga pulsar were conducted between January 2017 to March 2019. The invention of the Sum-Trigger-II system led to this successful detection, for it enhances the sensitivity of the MAGIC telescopes in the energy range of 10 GeV to 100 GeV (Dazzi et al., 2021). The observations were taken in the wobble mode, in which the telescopes were pointed to positions around the source with an offset of 0.4 degrees (Fomin et al., 1994) (See Sec. 2.1 for more details). Each run corresponds to a specific wobble position and typically lasts for 20 minutes. After quality selection, data from 270 runs were collected in 54 nights of observations, with a total effective time of approximately 80 hours.

The low-level analysis of Geminga data was previously performed with MARS in Ceribella (2021), following a similar procedure as in the previous chapter. Events were extracted and calibrated using `Sorcerer`, with MaTaJu cleaning applied to select relevant pixels. The bright star Alhena ($m_V = 1.92$) in the field of view was masked to accurately calculate the image parameters. The physical parameters were estimated using `Melibea`, with random forest estimators trained on off-observations and Monte-Carlo (MC) simulations. The pulsar phases were computed using ephemeris derived from *Fermi*-LAT data.

The fully-analyzed melibea files contain information on the energy, direction, phase, and particle type of the events. They are the basis for high-level scientific results, such as light curves and energy spectra. While the previous steps are specific to the instrumentation and detection technique of each observatory, it is possible to perform high-level analysis on the calibrated data using a different software tool, such as `Gammapy`.

3.2 Gammapy data reduction

Converting data to DL3 files

In this work, the Gammapy analysis started with Geminga melibea files, supplemented

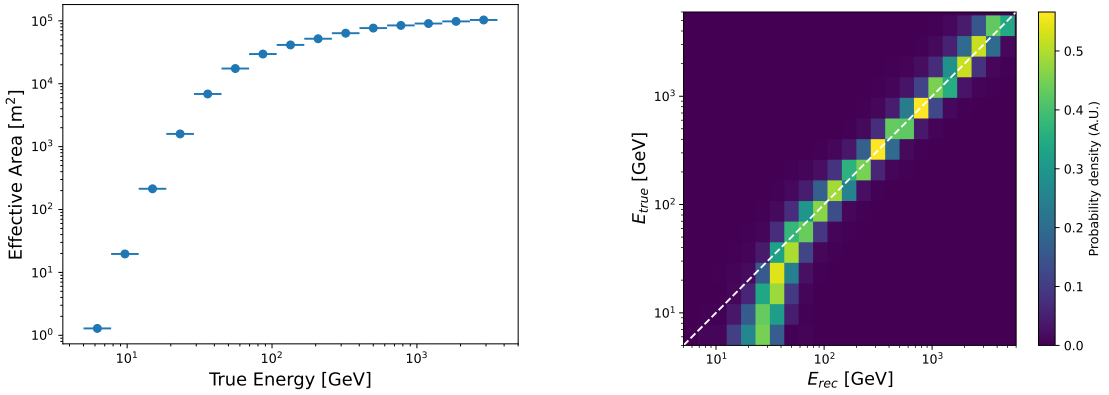

Figure 3.1: Instrument response functions for the MAGIC Geminga data obtained using DL3 converter. For the 1D analysis with ring-wobble MC files, the IRFs include the effective area (left) and the energy migration matrix (right).

with Monte-Carlo simulations tailored for the low-energy pulsar analysis (see Sec. 2.2.3). They were used to produce the data-level-3 (DL3) files in the flexible image transport system (FITS) format (Pence et al., 2010), which contain lists of gamma-ray-like events with estimated physical parameters and instrument response functions (IRFs).

For conversion of MAGIC data, we employed the MAGIC DL3 converter[3], a C++ library built on ROOT (Brun and Rademakers, 1997), MARS, and CFITSIO (Pence, 1999) that converts melibea ROOT files to DL3 FITS files (Abe et al., 2024). Fig. 3.1 shows the instrument response functions obtained from the Monte-Carlo events using the DL3 converter for the user-specified energy binning. The analysis cuts on hadronness and θ^2 were optimized for gamma-ray efficiencies of 90% and 75%, respectively. The results are presented in Fig. 3.2. For each observation run, an event list was generated after applying the analysis cuts. It contains information of position, time duration, hadronness, and energy.

Adding phase information

For pulsar analysis, we further added phase information to each event in the DL3 files, which is a step not included in the DL3 converter. This was done by matching the event IDs in DL3 files to those in melibea ROOT files. The python script is provided in Appendix D. Fig. 3.3 shows the phaseogram of the Geminga pulsar with energy-dependent analysis cuts produced by DL3 converter. The phase regions for the P1 and P2 pulsed components, as well as the off region, were determined from *Fermi*-LAT data. There is a significant detection of the P2 pulsed emission, at the significance level of 6.04σ. This is consistent with previous MARS result of 6.3σ, obtained using cuts produced by `Flute` with the same gamma-ray efficiencies.

[3] `https://gitlab.pic.es/magic_dl3/magic_dl3`

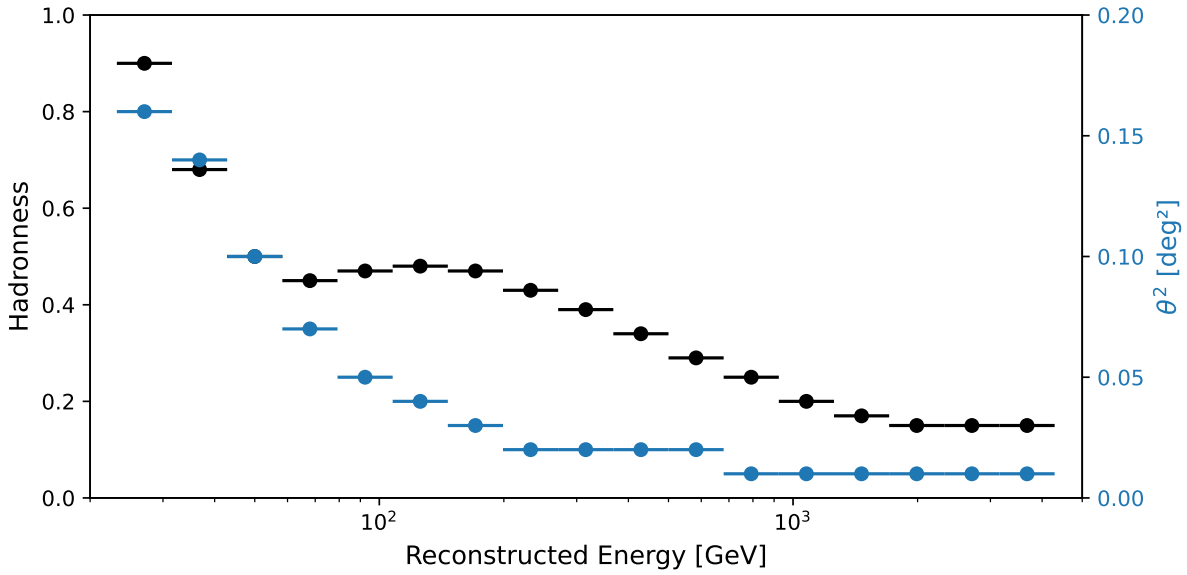

Figure 3.2: Hadronness (black) and θ^2 (blue) cuts obtained using the DL3 converter with gamma-ray efficiencies of 90% and 75%, respectively. (see Sec. 2.3.2 for more discussions)

Data reduction with Gammapy

Finally, binned datasets were created from DL3 files using `PhaseBackgroundMaker` in `Gammapy`. Its energy binning should be the same as those used in the DL3 converter for IRF computation. To analyze the spectrum of the pulsed emission, the on and off counts in each reconstructed energy bin were extracted from the P2 phase region (0.550–0.642) and the off-pulse region (0.700–0.950), respectively. The background was estimated from the off counts by multiplying the ratio of exposure between the on and off regions. Here the ratio is $\alpha = 0.368$. Correspondingly, the number of excess counts in each energy bin is given by $N_{\text{excess}} = N_{\text{on}} - \alpha N_{\text{off}}$. As the result of Gammapy data reduction, Fig. 3.4 shows the distributions of signal, background and excess counts in the stacked dataset. They are the basis of spectral analysis.

3.3 Spectrum fitting

The goal of spectrum fitting is to constrain the parameters of given spectral model, which can provide insights into the radiation mechanism of the source. In this work, we consider the following two basic analytical models:

1) The power law spectral model: the simplest analytical model, which is a straight line

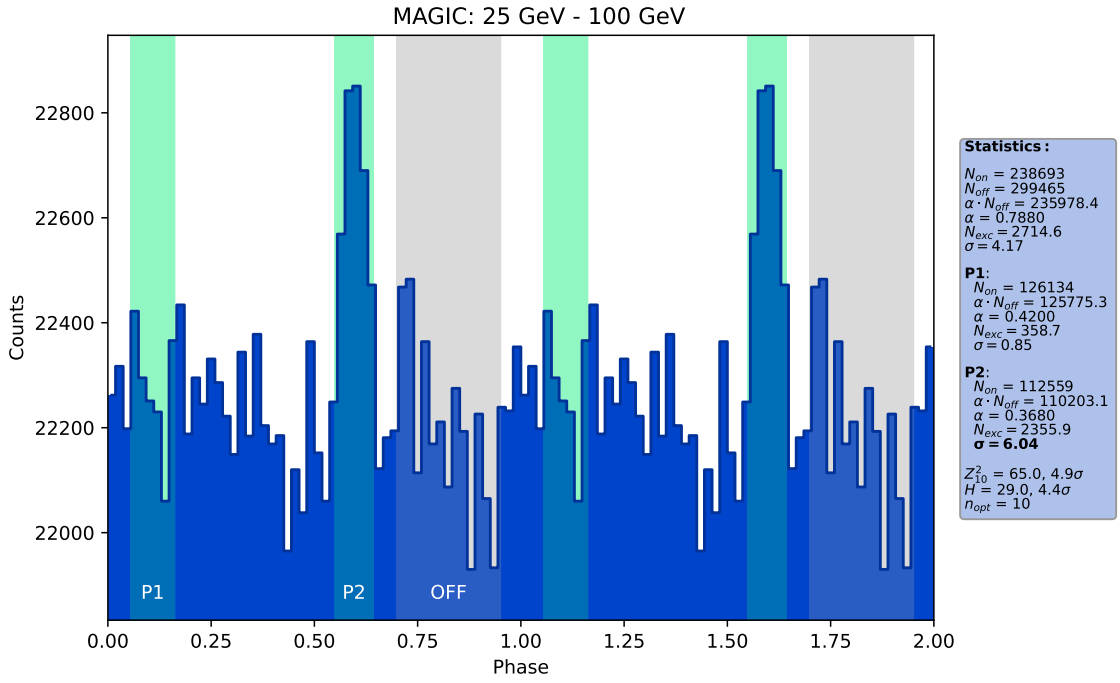

Figure 3.3: Phaseogram of the Geminga pulsar in the reconstructed energy range of 25 GeV to 100 GeV, corresponding to $\sim 15 - 100$ GeV in the true energy range. The hadronness and θ^2 cuts produced by DL3 converter are applied. The green shaded regions highlight the P1 and P2 pulsed emissions, determined from *Fermi*-LAT data in the 1 GeV – 15 GeV energy range. The off-pulse region used for background estimation is shown in gray. The P2 pulse is detected at the 6.0σ significance level.

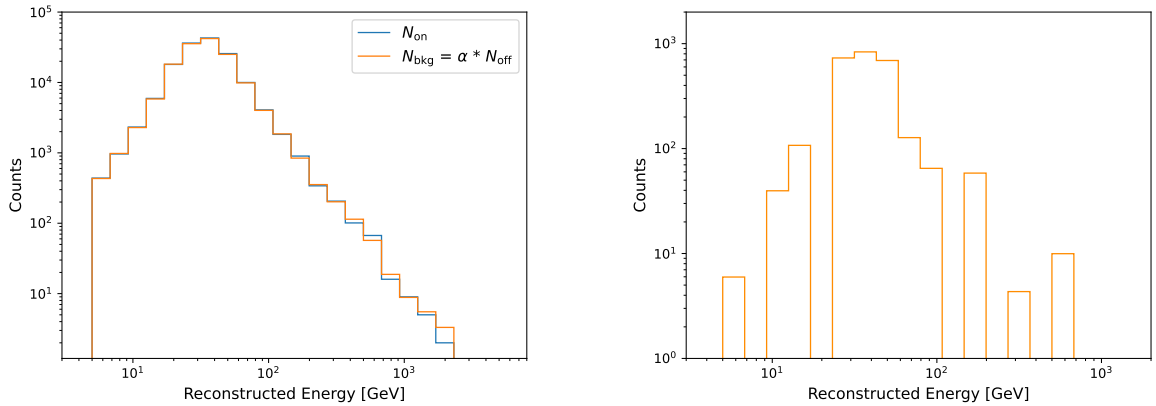

Figure 3.4: Distributions of event counts obtained from MAGIC Geminga observations with Gammapy. Left: the signal (blue) and background (orange) count distributions. Right: the excess count distribution, which is the difference between the signal and background count distributions.

	f_0	Γ	β
Power-law (Gammapy)	$(2.35 \pm 0.59) \times 10^{-9}$	5.17 ± 0.39	0 (fixed)
Log-parabola (Gammapy)	$(3.01 \pm 1.18) \times 10^{-9}$	5.7 ± 1.4	1.09 ± 1.94
Power-law (MARS)	$(2.28 \pm 0.74) \times 10^{-9}$	5.62 ± 0.54	0 (fixed)

Table 3.1: Best-fit parameters for the power-law and log-parabola models of the Geminga P2 emission obtained with Gammapy and MARS. The reference energy is $E_0 = 32.15$ GeV , at which the parameters have the minimum correlation. The unit of reference flux f_0 is $\mathrm{TeV}^{-1}\,\mathrm{cm}^{-2}\,\mathrm{s}^{-1}$. The large uncertainties in β indicates that a curved spectrum is not preferred.

in logarithmic space. It is given by

$$\phi(E) = f_0 \cdot \left(\frac{E}{E_0}\right)^{-\Gamma} , \tag{3.1}$$

where $\phi(E)$ is the differential flux, E_0 is the reference energy, and Γ and f_0 are two free parameters representing spectral index and the reference flux at E_0, respectively.

2) The log parabola spectral model: the simplest model to investigate potential curvature in the spectrum, defined as

$$\phi(E) = f_0 \cdot \left(\frac{E}{E_0}\right)^{-\Gamma-\beta\ln(\frac{E}{E_0})} , \tag{3.2}$$

with a free parameter β to parameterize a curve in logarithmic space. The power law model is a special case of the log parabola model with $\beta = 0$.

The above spectral models were fitted to the reduced datasets using the `Fit` class. It works with different backends, and the default minimizer `iminuit` (Dembinski et al., 2020) was chosen in this work. Starting from the spectral model, a forward-folding approach was applied to obtain the expected distribution of excess counts in bins of reconstructed energy, as illustrated in Fig. 3.5. Assuming Poisson statistics in each energy bin, the joint likelihood was given by the W statistics (Arnaud et al., 2022). By maximizing the Poisson likelihood, the best-fit parameters can be obtained finally. The detailed fit statistics is provided in Appendix B.

Fig. 3.6 shows the spectrum fitting results for the Geminga P2 emission. The shaded regions represent the 1σ statistical uncertainty of the fits. The best-fit parameters and their uncertainties are summarized in Table 3.1. In Fig. 3.6, there are large uncertainties in the parameters of the log-parabola model, implying that the observations are unable to determine the curvature of the spectrum, and a more complex model is not necessary at the current stage. This is further supported by the likelihood-ratio test. The test statistic (TS) between the power-law and the log-parabola model is $\mathrm{TS} \equiv -2\Delta \ln \mathcal{L} = 1.03$ with 1 degree of freedom. It corresponds to a p-value of 0.31, indicating that there is no

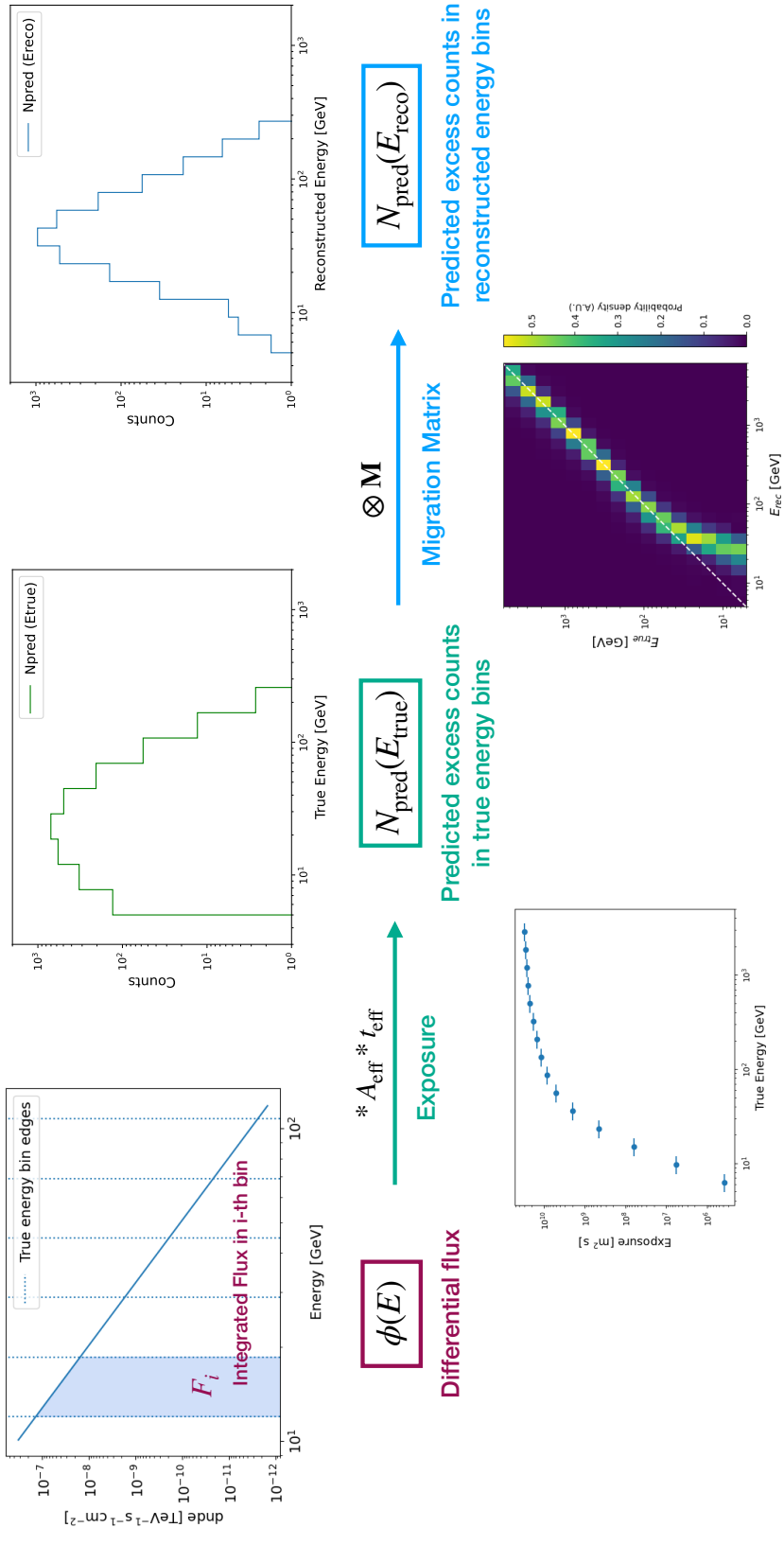

Figure 3.5: Schematic of the forward-folding process, where the spectral model is convolved with instrument response functions to obtain the predicted counts. In this work, both spectrum fitting and flux point estimation rely on the forward-folding approach. For the MCMC-based technique described in Sec. 3.4, the spectral model would be the stepped power law model, and the predicted count distribution is important for the calculation of the regularization term.

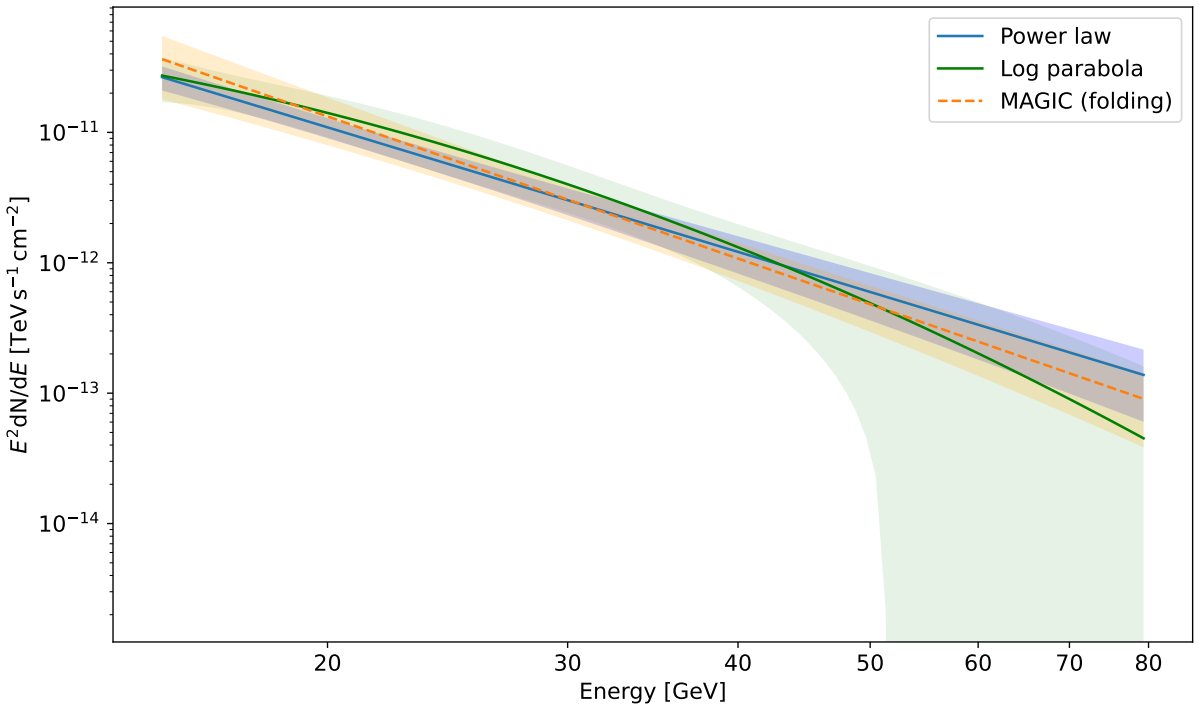

Figure 3.6: Spectrum fitting results for the P2 emission of the Geminga pulsar to a power-law model (blue) and a log-parabola model (green) with Gammapy. The power-law fit obtained with Gammapy Fit is consistent with the previous result from the MARS program Fold (orange), which also applies a forward-folding approach. The shaded bands represent the 1σ statistical uncertainties. There is no significant reference for a curved spectrum.

significant preference for a curved spectrum. Therefore, the P2 emission of the Geminga pulsar is well-described by the power-law model with a spectral index $\Gamma = 5.17 \pm 0.39$.

In addition, the power-law fit results with `Fit` were compared with those obtained previously from the same data using the MARS program `Fold`. The discrepancy can be roughly quantified as

$$\frac{\Gamma_{\mathrm{MARS}} - \Gamma_{\mathrm{Gammapy}}}{\sqrt{\sigma^2_{\mathrm{MARS}} + \sigma^2_{\mathrm{Gammapy}}}} = 0.68 \ , \tag{3.3}$$

which is close to the parameter uncertainty. Therefore, the spectrum fitting results from `Gammapy` are consistent with those from MARS. This is expected, as both methods rely on a similar forward-folding procedure.

3.4 Improvement of the flux point estimation technique

In contrast to spectrum fitting in the previous section, which aims to constrain parameters for a specific model, the goal of flux point estimation is to obtain discrete spectral points and their correlation matrix, which allow us to fit with arbitrary functions. This can be achieved using an unfolding approach, as in the MAGIC analysis with software `ComUnfold`, or using the forward-folding method, as implemented in `Gammapy`.

The performance of Gammapy's standard estimator is discussed in Sec. 3.4.1, and two main issues are identified. To address these issues, the stepped power law model is proposed in Sec. 3.4.2. However, directly fitting the model parameters will lead to large uncertainties, due to the ill-posed nature of the problem. To achieve robust flux point estimation, the MCMC technique with Tikhonov regularization is developed, as described in Sec. 3.4.3.

3.4.1 Limitations of Gammapy's standard estimator

In `Gammapy`, flux point estimation is based on a forward-folding procedure. The flux is estimated in each energy bin by freezing the shape of the reference spectrum and adjusting a normalization parameter to maximize the likelihood of the predicted counts.

Fig. 3.7 shows the spectral points for the Geminga pulsar obtained using Gammapy's standard estimator `FluxPointsEstimator`. The corresponding reference spectrum for the forward-folding analysis is the best-fit power law model obtained previously. Compared to the MAGIC unfolding results, this approach shows uneven energy binning, and fails to estimate the lowest-energy flux point.

To understand this behavior, the detailed analysis procedure was investigated, as illustrated

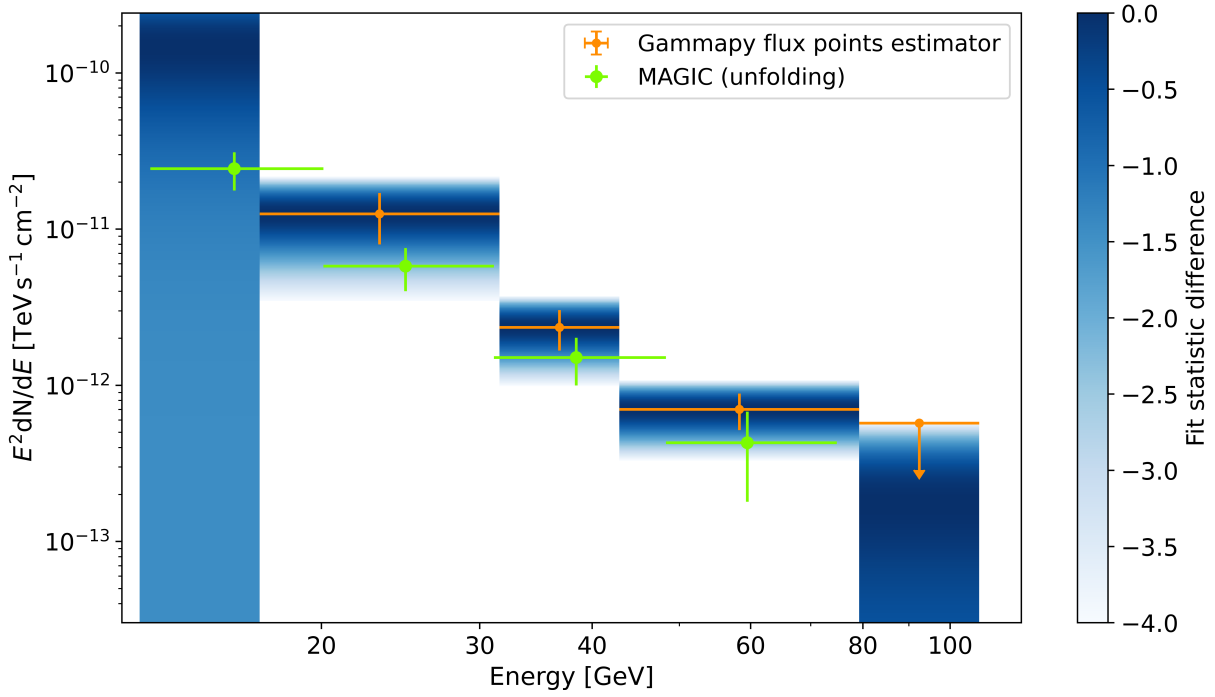

Figure 3.7: Spectral flux points and their likelihood profiles for the Geminga pulsar with Gammapy flux points estimator via forward folding. Results obtained from MAGIC analysis with unfolding procedure are shown in green for performance comparison.

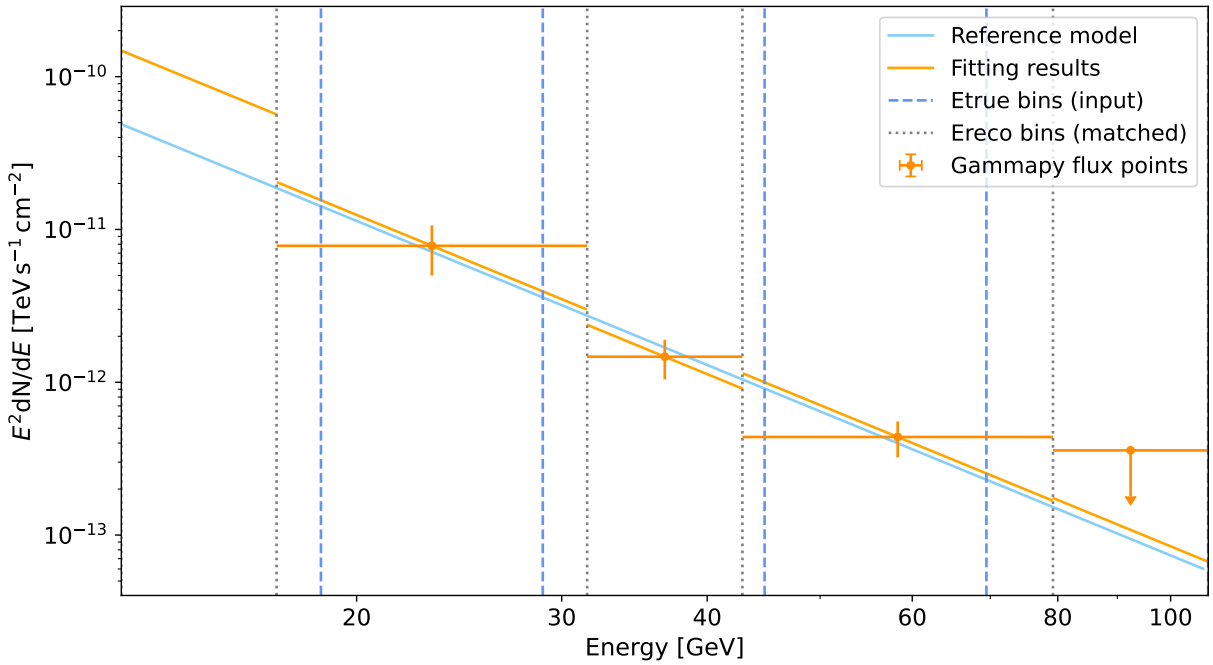

Figure 3.8: Illustration of the flux point estimation procedure in Gammapy. The input energy bin edges (blue dashed) are matched to the closest reconstructed energy bin edges (gray dotted). With the shape of the reference spectral model fixed, the normalization parameter is fitted in each sliced bin independently. The spectral points are evaluated at the logarithmic bin centers.

in Fig. 3.8. It starts with a predefined reference spectral model, slices the model and dataset into many energy bins, and fits the amplitude of the reference model in each energy bin independently. In each bin, the shape of the spectral model is fixed, and the amplitude is re-normalized using a 'norm' parameter, which describes the deviation of the flux from the reference model. The flux points are evaluated at the logarithmic bin centers $\sqrt{E_i E_{i+1}}$ based on the fitted normalization, and the 1σ errors are computed from the likelihood profile.

From the internal process described above, we identified two potential issues with Gammapy's `FluxPointEstimator`. First, allowing an arbitrary predefined reference spectral model can be problematic. The sliced reference spectrum in each bin may have different shapes with a log parabola model, which would lead to unwanted model-dependence and correlations between bins.

The second issue is about the energy binning, whose impact on the bin width and analysis threshold can be found in Fig. 3.7. The analysis should be performed in the true energy space, rather than the reconstructed energy space. However, in the slicing process, the input true energy bin edges will be automatically matched to the closest edges of recon-

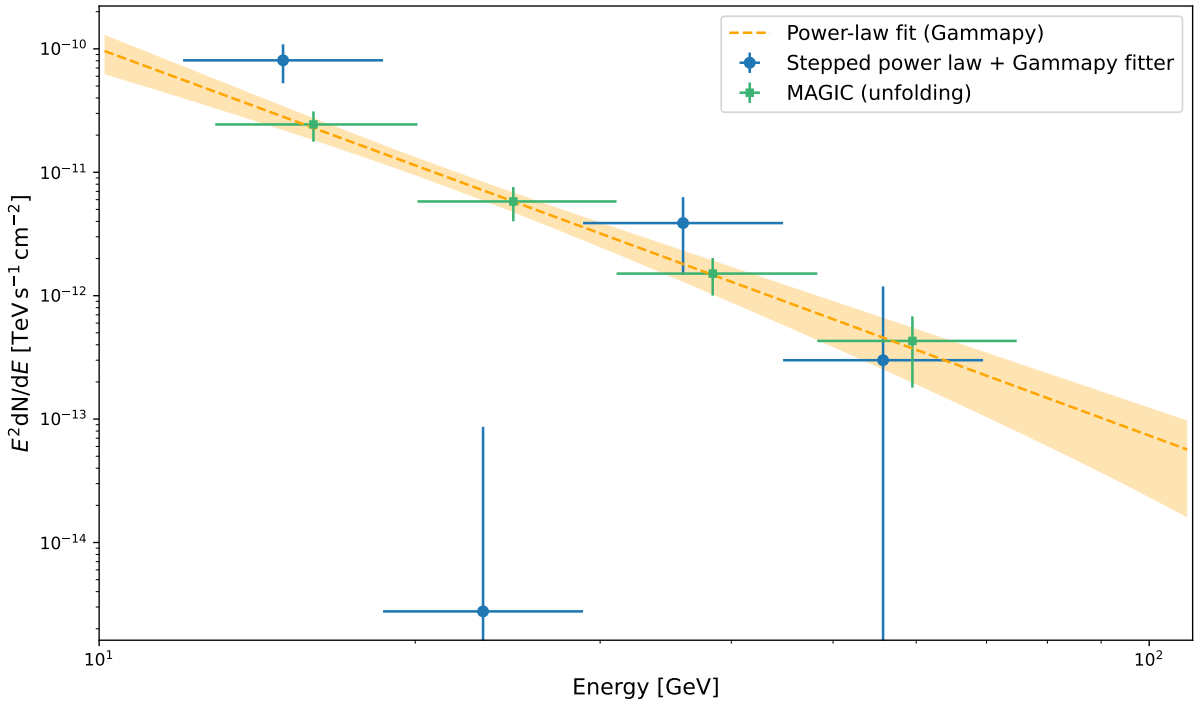

Figure 3.9: Spectral points for the Geminga pulsar obtained from maximum-likelihood fitting with a stepped power law model via forward folding. The resulting spectral points show large uncertainties compared to those obtained from MAGIC unfolding analysis (green). The orange dashed line represents the previous spectrum fitting results for the power law model.

structed energy bins, as is shown in Fig.3.8. Performing analysis in the reconstructed energy space will lead to unreliable results on the edge of the underlying spectrum, and may even fail to estimate the lowest-energy flux point, due to the energy estimation bias from low-energy events being reconstructed into higher energies.

3.4.2 Fitting the stepped power law model as a solution

The stepped power law model

To address the above issues, a stepped power law model was proposed as the reference spectrum in the forward-folding procedure. This model keeps the power-law index fixed (e.g., $\Gamma = 2$), treating the normalization factors in *true energy* bins as free parameters. The differential flux in the i-th true energy bin is then described as:

$$\phi_i(E) = N_i \cdot f_0 \cdot \left(\frac{E}{E_0}\right)^{-2} , \tag{3.4}$$

where E_0 is the reference energy, f_0 is the reference flux, which can be set to the previous best-fit value, and N_i is the corresponding free normalization parameter, which is an estimate of the flux point.

Obtaining model parameters with maximum likelihood fit

After selecting an energy range that covers bins with significant excess counts, the normalization parameters can be obtained by performing a maximum likelihood fit with Gammapy `Fit` in the true energy space.

Fig 3.9 shows the resulting flux points for the Geminga pulsar. There are very large uncertainties in the fitted normalization parameters. In addition, the flux points show an unnatural up-and-down pattern between adjacent bins. This suggests that the fitter may be potentially trapped in a local minimum, and is unable to find the optimal solution.

The reason why the stepped power law model with Gammapy fitter fails to provide robust results is due to the ill-posed nature of the problem. This means that the problem either does not have a unique solution, or the solution is unstable to the measurements, similar to the situation in the unfolding method. It can be mathematically proved that the noise components in the energy migration matrix can introduce significant noise in the resulting flux point estimation, and enhance the correlations between adjacent bins, as discussed in more detail in Wittek (2006) and summarized in Appendix C.

In order to suppress the noise components and reduce the correlations, a regularization method is introduced in the next section.

3.4.3 MCMC analysis with Tikhonov regularization

The direct fitting of the stepped power law model is limited by the ill-posed nature of the problem. To obtain robust flux point estimation with `Gammapy`, we implemented the MCMC technique with an additional regularization term for the stepped power law model. After introducing the theoretical framework, the implementation details are provided at the end of this section.

MCMC in Bayesian analysis

According to Bayes' theorem, constraints on the model parameters given the measurements can be derived as

$$\mathcal{P}(\theta|d) = \frac{\mathcal{L}(d|\theta)\,\pi(\theta)}{\mathcal{Z}}\ , \tag{3.5}$$

where θ is a set of model parameters, d is the measured data. In Bayesian data analysis, the model parameters are treated as random variables, and their probability density function is the posterior $\mathcal{P}$, given by the product of likelihood $\mathcal{L}$ and prior π, with a normalization

factor $\mathcal{Z}$ called 'evidence'. The posterior represents our updated knowledge on the parameters: the previous knowledge given in prior is updated with new information provided by likelihood.

To estimate the posterior, we can construct a sequence of points whose density is proportional to the posterior distribution. This can be achieved using Markov Chain Monte Carlo technique. A Markov chain is a sequence in which the i-th sampling point only depends on the $(i-1)$-th point. After a sufficient number of steps, or the 'burn-in' phase, it will reach a stationary distribution, in our case the posterior distribution.

Tikhonov regularization

To solve the ill-posed optimization problem, we add a regularization term $R(B)$ to the χ_0^2, which is equivalent to adding extra constraints on the solution:

$$\chi^2 = \chi_0^2 + \lambda R(B) \ , \tag{3.6}$$

where B is the solution, and λ is a free parameter that controls the effect of regularization. In the following we will name it as 'regularization depth'. The term $\lambda R(B)$ will penalize some unwanted features, such as the up-and-down pattern shown in the previous section, thus enabling us to obtain the unique optimal solution.

There are various choices for the regularization term. Among them, the Tikhonov regularization (Tikhonov, 1963), a method with simple analytical form, is a very effective technique for the least squares problem. Applying it we have

$$-2\ln\mathcal{L}' = -2\ln\mathcal{L}_0 + \lambda\|\Gamma B\|^2 \ . \tag{3.7}$$

where $\mathcal{L}_0$ is the previous likelihood, $\mathcal{L}'$ is the likelihood after adding the regularization term, $\|\cdot\|$ is the L2 norm, and the Tikhonov matrix Γ is an operator acting on the parameter vector. If one chooses it to be the identity matrix $\Gamma = \mathbf{I}$, then solutions with smaller norms will be preferred. It can also be difference operators, which will enforce the smoothness of the solution.

Here since the underlying distribution B is believed to be mostly continuous, we choose the second derivative of $\ln B$ as the Tikhonov regularization term to constrain the curvature of B:

$$R(B) = \|\frac{d^2\ln B}{dx^2}\|^2 = \sum_{j=2}^{n_b-1}\left[2\cdot\left(\frac{B_{j+1}-B_j}{B_{j+1}+B_j} - \frac{B_j - B_{j-1}}{B_j + B_{j-1}}\right)\right]^2 \ . \tag{3.8}$$

The Bayesian interpretation of the regularization term for the ill-posed problem can be understood in the following way. By inserting Eq. 3.6 to Eq. 3.5, we have

$$\mathcal{P} \propto \exp\left(-\frac{1}{2}\left(\chi_0^2 + \lambda R(B)\right)\right) \propto \mathcal{L}_0 \cdot \pi_R \ , \tag{3.9}$$

with

$$\pi_R = \exp\left(-\frac{\lambda}{2}R(B)\right) \ , \tag{3.10}$$

suggesting that the regularization term corresponds to a prior in the Bayesian framework.

For the Tikhonov regularization,

$$\pi_R = \exp\left(-\frac{\lambda}{2}B^T\Gamma^T\Gamma B\right) \ , \tag{3.11}$$

implying that it can be further approximated as a multivariate Gaussian distribution.

Criterion for the optimal regularization depth

The result of maximum likelihood estimation depends on the choice of regularization depth λ. A λ that is too small is unable to solve the ill-posed problem, while a λ that is too large will lead to an overly smooth solution, which is a biased estimate of the true distribution.

There are various criteria for determining the optimal regularization depth to balance the bias-variance trade-off. However, there is no universal solution that applies to all situations, since the choice of the optimal λ_{opt} depends on the shape of the unknown true solution B. The criterion we use here follows the one in `ComUnfold` (Wittek, 2006), which involves the traces of relevant covariance matrices:

$$Tr(\mathbf{C_A}) = Tr(\mathbf{C_B}) \ , \tag{3.12}$$

where $\mathbf{C_A}$ and $\mathbf{C_B}$ are the covariance matrices of the input measurements and the output estimation, respectively.

The matrix $\mathbf{C_A}$ only consists of diagonal terms $\sigma^2_{A_i}$, which represent the variance of measured excess counts in bins of reconstructed energy, given by

$$\sigma_{A_i} = \sqrt{N_{\text{on,i}} + \alpha^2 N_{\text{off,i}}} \quad (i = 1, \ldots, n_a) \ . \tag{3.13}$$

Here we assume $N_{\text{on,i}}$ and $N_{\text{off,i}}$ have Poisson errors and are independent of each other.

For $\mathbf{C_B}$, the diagonal terms are the uncertainties of the predicted counts in bins of true energy. $\mathbf{C_B}$ is derived from MCMC results using error propagation:

$$\mathbf{C_B} = \mathbf{J_B} \cdot \mathbf{C}_{\text{norm}} \cdot \mathbf{J_B}^T \ , \tag{3.14}$$

where the Jacobian matrix has elements $(\mathbf{J_B})_{jk} = (\frac{\partial B_j}{\partial \text{norm}_k})$, estimated numerically using the local gradients. $\mathbf{C}_{\text{norm}}$ is the covariance matrix of the best-fit normalization parameters, obtained from the MCMC chains.

In conclusion, the criterion for λ_{opt} given in Eq. 3.12 reflects the trade-off between large noise and strong bias. As increasing λ leads to stronger regularization and smaller $Tr(\mathbf{C_B})$, requiring this criterion means that we want to reduce the noise components caused by the ill-posed nature of the problem to a certain reasonable level, quantified here by $Tr(\mathbf{C_A})$.

Implementation of the MCMC technique with Tikhonov regularization

According to the theoretical framework described above, we developed an analysis pipeline employing MCMC sampling with Tikhonov regularization for flux point estimation. The codes are available in a public git repository (see Appendix D).

The technique was built on an existing script from the Gammapy Recipes[4], which implemented MCMC sampling for spectral model parameters using the emcee package. We extended this work by incorporating the stepped power law model and the Tikhonov regularization, in order to achieve the different purpose of flux point estimation.

The implementation involved the following processes:

- Introducing the stepped power law model: since this model was not available in the standard `Gammapy`, it was defined according to Eq. 3.4, and served as the reference spectral model
- Implementing MCMC sampling with Tikhonov regularization for a given regularization depth λ: the Tikhonov regularization term $R(B)$ was added to the likelihood function as described in Eq. 3.7. The predicted counts distribution B was obtained from the forward-folding procedure, as in illustrated in Fig. 3.5.
- Determining the optimal regularization depth $\lambda_{\rm opt}$ according to the criteria given in Eq. 3.12: multiple MCMC runs with varying λ were performed by a separate python script, which calculated $Tr(\mathbf{C_A})$ and $Tr(\mathbf{C_B})$ for each λ (see Eq. 3.13 and Eq. 3.14 for the calculation). To accurately determine the $\lambda_{\rm opt}$, the relation between λ and the ratio of $Tr(\mathbf{C_A})$ and $Tr(\mathbf{C_B})$ was fitted.
- Final flux point estimation: the MCMC sampling with $\lambda_{\rm opt}$ was performed to determine the normalization parameters in the stepped power law model. The corresponding SED values were calculated according to Eq. 3.4.

3.5 Flux point estimation results using the new technique

The spectral points for the Geminga pulsar were estimated with the new analysis pipeline described above. The optimal regularization depth was determined from the criterion given in Eq. 3.12 by fitting the relationship between λ and the ratio of $Tr(\mathbf{C_B})$ and $Tr(\mathbf{C_A})$ (Fig. 3.10). The optimal regularization depth for the Geminga data is 0.68.

[4] `https://gammapy.github.io/gammapy-recipes/_build/html/notebooks/mcmc-sampling-emcee/mcmc_sampling.html`

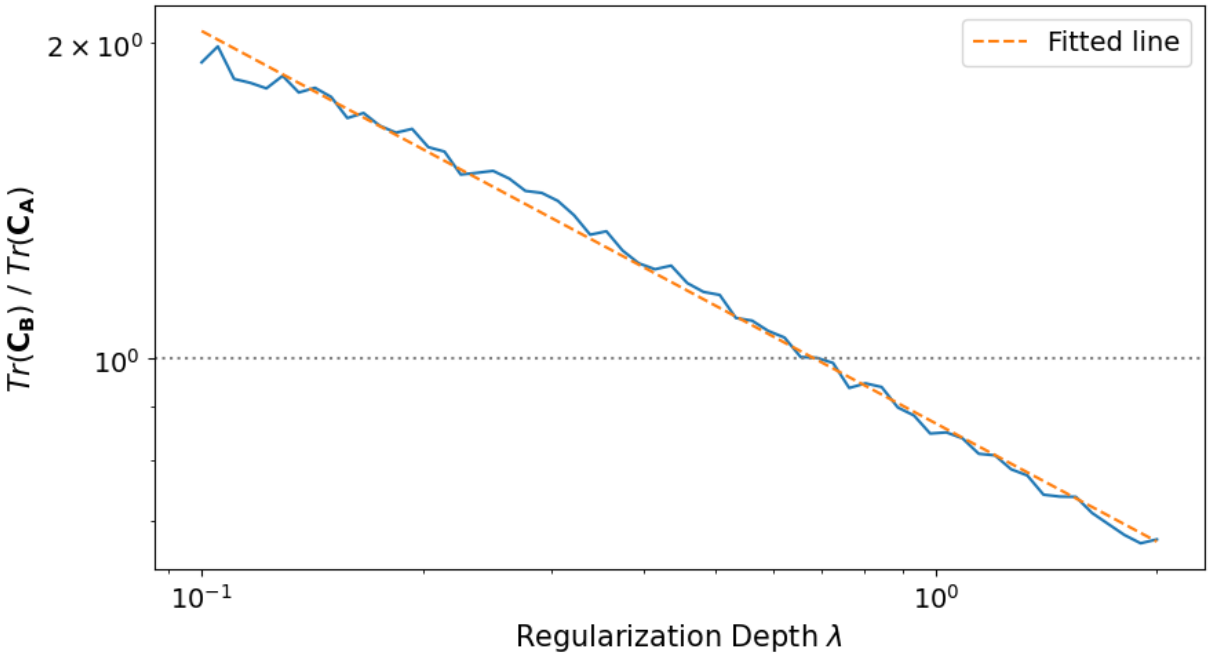

Figure 3.10: The ratio of $Tr(\mathbf{C_B})$ and $Tr(\mathbf{C_A})$ in multiple MCMC runs with varying regularization depths for Geminga data. The best-fit relation (orange) is used to determine the optimal regularization depth.

The effect of regularization term on the sampling process can be found by comparing the corner plots with or without regularization, as shown in Fig. 3.11. The corner plots show the two-dimensional marginalized distribution between every two normalization parameters, and the one-dimensional projection for each parameter. The estimates of the model parameters are given by the median, with negative and positive uncertainties based on the 68% credible interval, corresponding to the 16% and 84% percentiles of the samples in the marginalized distributions, respectively. After applying the optimal Tikhonov regularization, correlations between adjacent energy bins due to the ill-posed problem are greatly reduced.

Fig. 3.12 shows the spectral energy distribution (SED) of the P2 emission of the Geminga pulsar from the MCMC analysis with optimal regularization depth. The SED values of the flux points and their correlation matrix are summarized in Table 3.2 and Table 3.3. For the lowest-energy flux point, there is a slightly larger difference between this method and MAGIC unfolding analysis, due to the large noise at low energies. In general, the SED results for the Geminga pulsar are compatible with those previously obtained from MARS.

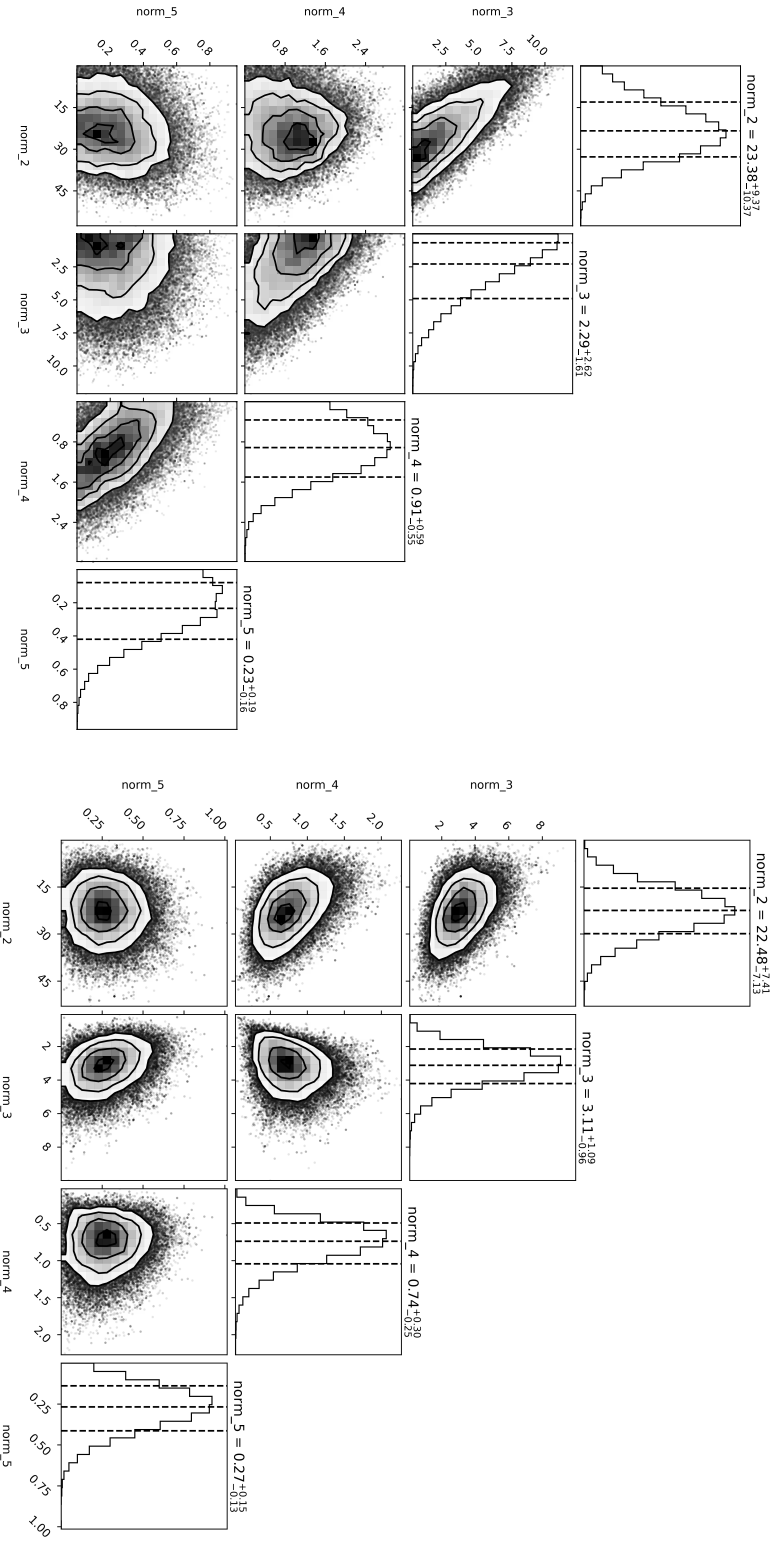

Figure 3.11: Comparison of corner plots for the MCMC analysis without regularization (left), and with optimal Tikhonov regularization (right). For the standard MCMC analysis, there are significant correlations between adjacent energy bins.

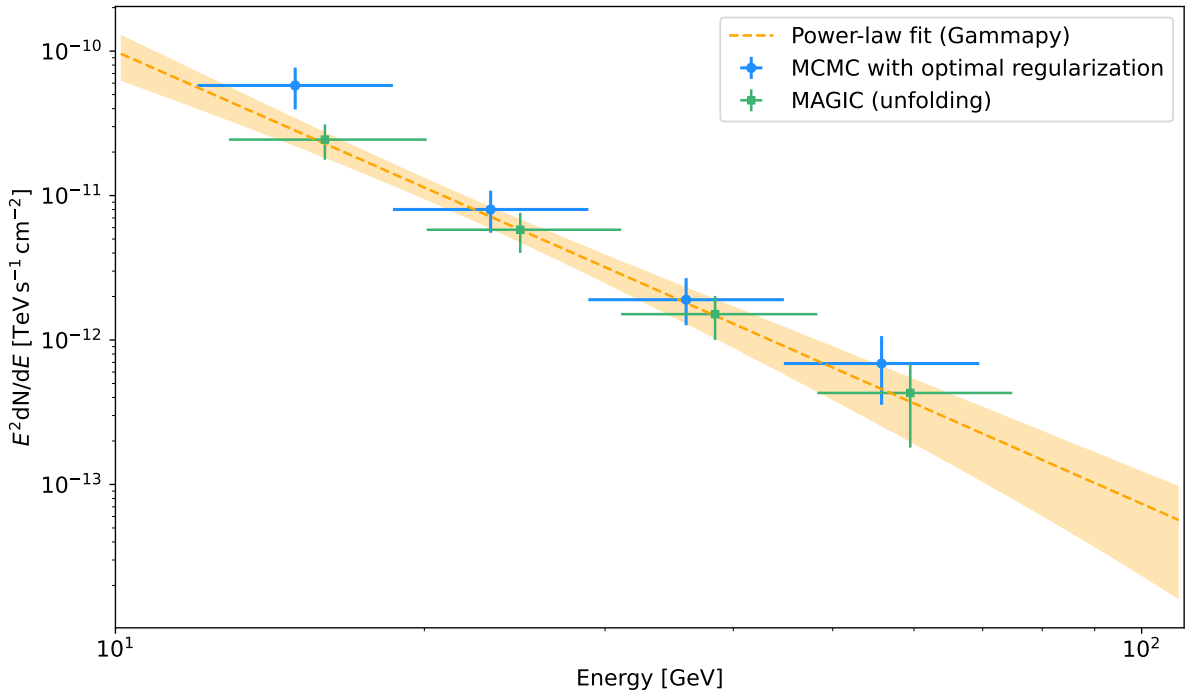

Figure 3.12: SED of the P2 emission of the Geminga pulsar from the MCMC-based analysis with Gammapy, which is consistent with MAGIC unfolding analysis (green). The spectral points are evaluated from the stepped power law model, with parameters estimated using MCMC analysis with optimal Tikhonov regularization. The orange dashed line shows the maximum Poisson likelihood fitting for the power-law model, with shaded region representing its 1σ uncertainty.

Flux Points	E_{low} (GeV)	E (GeV)	E_{high} (GeV)	SED (TeV cm^{-2} s^{-1})
1	12.0	15.0	18.6	$(5.78^{+1.91}_{-1.83}) \times 10^{-11}$
2	18.6	23.2	28.9	$(8.01^{+2.80}_{-2.48}) \times 10^{-12}$
3	28.9	36.0	44.8	$(1.90^{+0.78}_{-0.64}) \times 10^{-12}$
4	44.8	55.8	69.5	$(6.87^{+3.77}_{-3.31}) \times 10^{-13}$

Table 3.2: Flux points for the Geminga P2 emission, obtained using MCMC analysis with optimal Tikhonov regularization. The energy bin edges are E_{low} and E_{high}. The SED values are evaluated at their logarithmic centers.

	1	2	3	4
1	1	-0.46	-0.47	0.05
2	-0.46	1	0.21	-0.31
3	-0.47	0.21	1	-0.09
4	0.05	-0.31	-0.09	1

Table 3.3: The correlation matrix between the spectral points.

	N_2	N_3	N_4	N_5
Gammapy fitter	31.39 ± 10.94	0.001 ± 0.03	1.51 ± 0.94	0.12 ± 0.35
MCMC	22.37 ± 10.14	-1.16 ± 4.02	0.80 ± 0.66	0.15 ± 0.23
MCMC+regularization	$22.48^{+7.41}_{-7.13}$	$3.12^{+1.09}_{-0.96}$	$0.74^{+0.30}_{-0.25}$	$0.27^{+0.15}_{-0.13}$

Table 3.4: Normalization parameters in the stepped power law model obtained from maximum-likelihood fitting using Gammapy fitter, standard MCMC without regularization, and MCMC with optimal Tikhonov regularization. Note that the estimation from the standard MCMC is biased, so here the mean and the standard deviation from Gaussian fit are applied.

3.6 Summary and discussion

In this chapter, we analyzed the MAGIC Sum-Trigger data of the Geminga pulsar with `Gammapy`, and obtained the spectrum of its pulsed emission P2, shown in Fig. 3.12.

For spectrum fitting, `Fit` performs the binned Poisson maximum likelihood fitting on the excess count distribution through a forward-folding procedure. The spectrum of the Geminga P2 emission is described by a power-law model with spectral index $\Gamma = 5.17 \pm 0.39$, which is consistent with the standard MAGIC analysis program `Fold`.

While `Fit` provides reliable parameter constraints, estimating flux points with `Gammapy` is very challenging, especially for data with low statistics and for sources with steep spectra. Two potential issues were found with the `FluxPointEstimator`: a) its dependence on a predefined reference spectrum may introduce unwanted correlations; b) the way it works in the reconstructed energy space is problematic, which can lead to unreliable results on the edge of the underlying spectrum.

We proposed the stepped power law model to address the above issues, where the flux points are evaluated from the normalization parameters in true energy bins. However, these parameters cannot be accurately determined with the normal maximum-likelihood fitting method such as `Fit`, due to the ill-posed nature of the problem.

To obtain robust flux point estimation, we implemented MCMC analysis with Tikhonov regularization. This forward-folding method provides results that are compatible with the

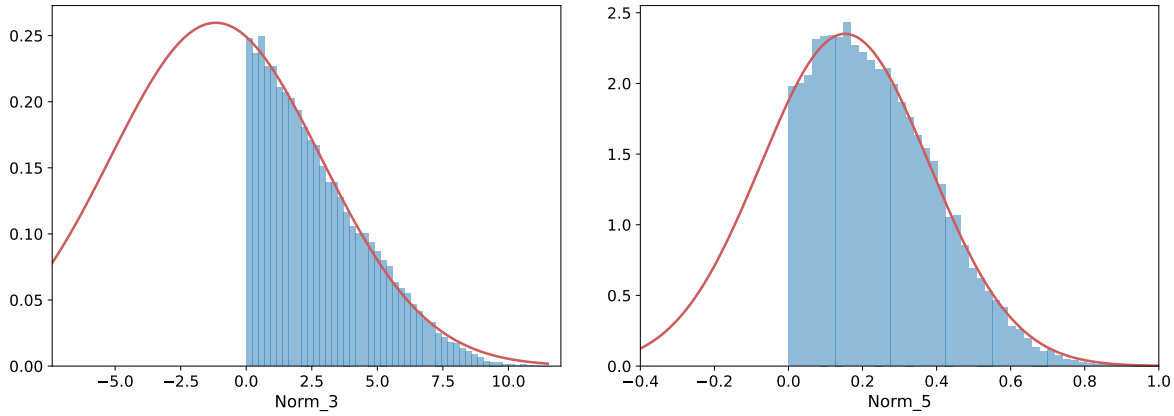

Figure 3.13: Gaussian fit (red) to the 1D marginalized posterior distribution (blue) from the standard MCMC without regularization for the second (left) and the fourth (right) flux points.

MAGIC unfolding program `ComUnfold`. The performance of this method is summarized in Table 3.4 and illustrated in Fig. 3.14. We should note that the estimation from the 16% and 84% percentiles of the samples in the standard MCMC without regularization is actually biased. For example, in the corresponding corner plot (Fig. 3.11), if we fit the 1D distribution of the second and the fourth flux point to a Gaussian distribution, we will obtain a much smaller mean and a much larger standard deviation (Fig. 3.13). In this case, the SED estimation will be the same as the results from Gammapy Fitter.

In future work, other regularization methods, such as reduced cross entropy (Schmelling, 1994), could be considered, with the optimal regularization depth determined by different criteria. This could help to reduce the remaining correlations (e.g., between the first and the third flux points) and further improve the robustness of flux point estimation.

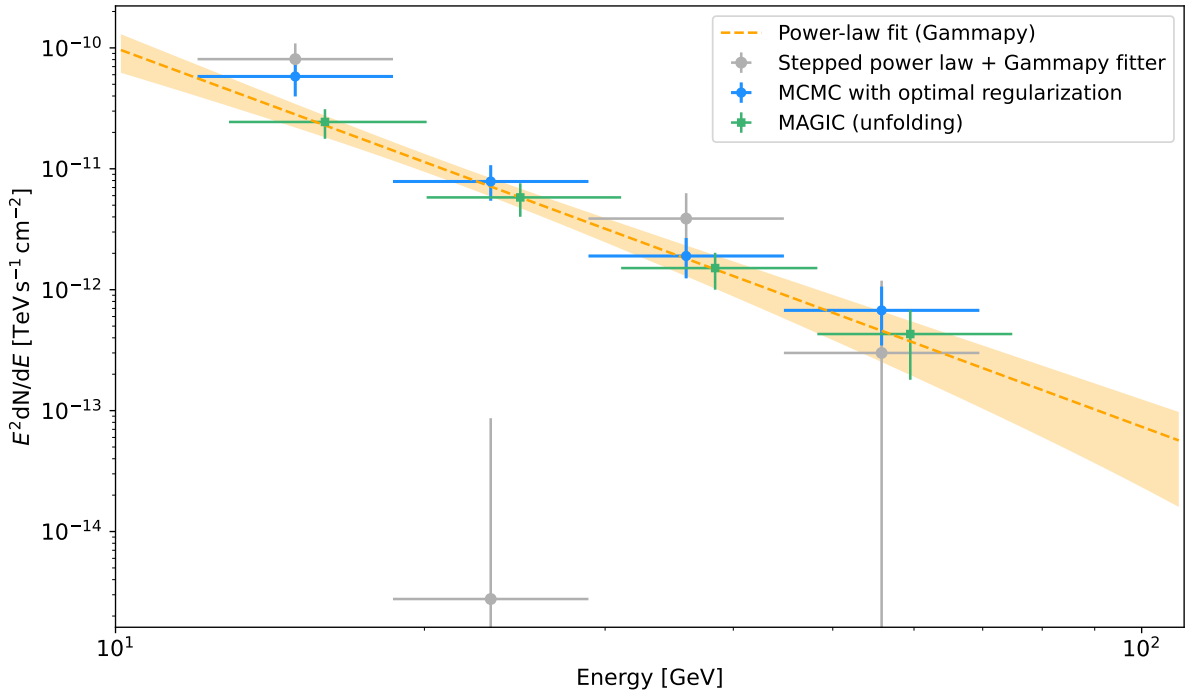

Figure 3.14: Flux points of the P2 emission of the Geminga pulsar, obtained with the stepped power law model using Gammapy fitter (gray) and MCMC with optimal Tikhonov regularization (blue). The spectral points from the standard MCMC without regularization are biased estimates and are not included in the plot (see text for details).

Chapter 4

Conclusion

This thesis studied the very-high-energy (VHE) emissions of two gamma-ray pulsars, the Dragonfly pulsar (PSR J2021+3651) and the Geminga pulsar (PSR J0633+1746) with observations from the Major Atmospheric Gamma Imaging Cherenkov (MAGIC) telescopes.

The VHE gamma-ray pulsations of the Dragonfly pulsar were investigated, using approximately 40 hours of MAGIC archival observations. During data reduction, the existing non-standard procedures for pulsar analysis were applied to better distinguish the low-energy signal from the dominating background noise. No significant pulsed component was found in the $30\,\mathrm{GeV} - 200\,\mathrm{GeV}$ energy range, at -0.55σ level from the Li & Ma significance. The non-detection was confirmed by the Z^2_{10} and H test, with detection significances of 1.0σ and 1.3σ, respectively.

The spectral features of the Geminga's pulsed component P2 were cross-checked using ~ 80 hours of MAGIC observations with `Gammapy` analysis. Robust flux points were obtained using the Markov Chain Monte Carlo (MCMC) analysis with Tikhonov regularization developed in this work. The spectrum is described by a power-law model with a spectral index of $\Gamma = 5.17 \pm 0.39$, which is compatible with previous MARS results of $\Gamma = 5.62 \pm 0.54$. The log-parabola model was also fitted, and no preference for a curved spectrum was found.

The gamma-ray emissions provide insights into the physical processes in the pulsar magnetosphere. The spectral results of Geminga confirmed the presence of a power-law tail in the spectrum of Geminga, as revealed by previous MAGIC analysis (MAGIC Collaboration, 2020), indicating a underlying inverse Compton process in the magnetosphere. However, for the younger and more energetic Dragonfly pulsar, no pulsed emission was detected. There is a possibility that the Dragonfly pulsar inherently does not produce the VHE gamma-ray pulsations. It is interesting to compare with the Vela pulsar, which shares similar properties with the Dragonfly. However, there is a main difference, which is the distance. The Dragonfly is approximately more than 10 times farther away than the Vela. For this reason, the limited observation time of ~ 40 hours may not have been sufficient

for detection. Therefore, future observations with longer exposures may help to reveal the potential VHE emissions.

We applied an MCMC technique with Tikhonov regularization for flux point estimation. It is based on the stepped power law model, proposed to address the two main issues with `FluxPointEstimator`, the standard method in `Gammapy`: a) its dependence on a predefined reference spectrum, which may introduce unwanted correlations; b) its operation in the reconstructed energy space, rather than the true energy space, which can lead to unreliable results on the edge of the underlying spectrum. Directly fitting the model parameters resulted in large uncertainties and correlations between adjacent energy bins, due to the ill-posed nature of the problem. Therefore, the Tikhonov regularization term was introduced to obtain reliable results, which can be interpreted as a prior with approximately multivariate Gaussian distribution in the Bayesian framework. This forward-folding-based technique is consistent with the results from the MAGIC unfolding method, providing robust estimates of spectral points.

Implementation of various forward-folding-based technique for `Gammapy` may help gamma-ray observations of pulsars with low statistics. In future work, other regularization methods, such as reduced cross entropy (Schmelling, 1994), can be considered, with the optimal regularization depth determined by different criteria.

Appendix A

Data reduction for the Dragonfly pulsar

This Appendix describes the technical details on the data reduction for the Dragonfly pulsar, with a focus on the application of MAGIC software.

Raw data processing

1. Preparation
    - The raw data (*_D_*.root): after quality selection, there are 13 nights of observations in July and 4 nights in August, 2014
    - Special data runs for each observation: a) calibration runs (*_C_*.root): runs with light pulses from the calibration box to estimate the calibration RMS ; b) pedestal runs (*_P_*.root) to estimate the baseline and pedestal RMS in calibration
    - Report files: information from the telescope subsystems, such as the drive system, trigger system, and camera
2. `Sorcerer`: Signal extraction, calibration, and MaTaJu cleaning
    - First run `Sorcerer` in C-mode, which loops over the calibration and pedestal files to compute the calibration conversion factor; then run in Y-model, which loops over the data files to perform data reduction.
    - MaTaJu cleaning is applied in the inputcard, whose parameters for each telescope follow the values in Table 4.1 in (Ceribella, 2021), which are optimized for the Crab and Geminga analysis

- In practice, this step involves running multiple specific Bash shell scripts to process a large number of files, written by Ceribella (2021).

3. Merge report files using `Merpp` with the gen_merpp.sh script

Image parametrization and stereo reconstruction

1. Image parametrization and bright star removal

   - `Star`: removing the bright stars and calculating image parameters
   - In the inputcard, specifying configuration parameters for bright star removal: a) MJStar.MStarPosCalc0.SourceRaDec: the star's RA and Dec coordinates; b) MJStar.MStarPixels0.StarRadius:the exclusion radius. The bright stars masked in this work is listed in Tab. 2.2.2
   - This step converts the calibrated files (*_Y_*.root) into files with Hillas parameters (*_I_*.root). In practice, it is done with gencom_star.sh script

2. Stereo reconstruction

   - `Superstar`: reconstruct the incident direction of the primary gamma ray
   - This step converts previous files (*_I_*.root) into files with stereo parameters (*_S_*.root). In practice, it is done with gencom_super.sh script

Physical Parametrization

1. `Coach` : training the Random Forest (RF) estimators

   - In the configuration file, specifying the training samples: a) gamma-ray events with tailored MC files, listed in Tab. 2.2; b) off observations: 15 observation runs of the Geminga pulsar.
   - Outputs:
     - The gamma/hadron separation forest: RF.root
     - The energy lookup tables (LUT): stored in Energy-Table.root
     - The energy estimation stereo RF: EnRF-Stereo.root
     - The stereo disp estimation forest : two DispRF.root for M1 and M2 (Note: these two files must have the same name, therefore should be stored in different directories: disp1 and disp2)

2. `Melibea`: applying random forests produced by `Coach` to estimate corresponding physical parameters to each event

- This step converts the files with stereo parameter (*_S_*.root) to *fully analyzed event files* (*_Q_*.root). In practice, it is done with gen_multibea.sh script

Pulsar phaseogram

1. Adding pulsar phase
   - Obtaining ephemeris from the Fermi pulsar catalog[1]
   - `Tempo2 plugin`: add phase and barycenteric time to each event. In practice, it is done with the run_tempo2.sh script
   - Note: should work on the *copy* of Melibea files, as there might be errors in phase calibration
2. Event selection
   - `Flute`: producing energy-dependent θ^2 and hadronness cuts, based on MC simulations different from those for RF training
   - Other high-level analysis with `Flute`:
     - In the configuration file, specifying parameters, such as the background mode, energy binning, gamma-ray efficiency, and the assumed intrinsic spectrum shape
     - More scientific products can be obtained, including excess count, θ^2 plot, energy migration matrix, effective area
3. Producing the phaseogram
   - After specifying the cuts file and the signal and background phase regions in the configuration file, the phaseogram can be produced with Phaseogram3.py, written by Ceribella (2021)

[1] `https://fermi.gsfc.nasa.gov/ssc/data/access/lat/3rd_PSR_catalog/3PC_HTML/`

Appendix B

Poisson likelihood maximization

Poisson statistics is used to describe the probability distribution of observed counts. It is important especially in the very low count regime, where the likelihood significantly deviates from Gaussian distribution.

Consider the Poisson likelihood with known background in the i-th bin of reconstructed energy. The probability of observing $N_{\mathrm{obs},i}$ counts in a given exposure time is

$$P(N_{\mathrm{obs},i}; N_{\mathrm{pred},i}) = \frac{(N_{\mathrm{pred},i})^{N_{\mathrm{obs},i}}}{(N_{\mathrm{obs},i})!}\, e^{-N_{\mathrm{pred},i}} \ , \tag{B.1}$$

where $N_{\mathrm{pred},i}$ is the number of expected counts given by the model.

Assuming the data in each bin is an independent draw from the Poisson distribution, the joint likelihood for N bins of reconstructed energy is

$$\mathcal{L} = \prod_{i=1}^{N} P(N_{\mathrm{obs},i}; N_{\mathrm{pred},i}) \ . \tag{B.2}$$

Taking the natural logarithm, we have

$$\ln \mathcal{L} = \sum_{i=1}^{N} [N_{\mathrm{obs},i} \ln N_{\mathrm{pred},i} - N_{\mathrm{pred},i} - \ln(N_{\mathrm{obs},i}!)] \ . \tag{B.3}$$

Neglecting the last term, which does not depend on model parameters, we arrive at the Cash statistics (Cash, 1979):

$$\mathcal{C} \equiv -2 \ln \mathcal{L} = 2 \sum_{i=1}^{N} (N_{\mathrm{pred},i} - N_{\mathrm{obs},i} \ln N_{\mathrm{pred},i}) \ . \tag{B.4}$$

In our case where the background also follows Poisson statistics but is not precisely known, we can introduce a nuisance parameter b_i, the expected Poisson counts of the background in the i-th bin. The likelihood becomes

$$\mathcal{P}(N_{\mathrm{on},i}, N_{\mathrm{off},i}\,; N_{\mathrm{pred},i}, b_i, \alpha) = \frac{(N_{\mathrm{pred},i} + \alpha\, b_i)^{N_{\mathrm{on},i}}}{(N_{\mathrm{on},i})!}\, e^{-(N_{\mathrm{pred},i}+\alpha\, b_i)} \cdot \frac{(b_i)^{N_{\mathrm{off},i}}}{(N_{\mathrm{off},i})!} e^{-b_i} \ , \tag{B.5}$$

where $N_{\mathrm{off},i}$ is the number of counts in the signal region, $N_{\mathrm{off},i}$ represents observed background counts, $N_{\mathrm{pred},i}$ is the number of predicted excess counts, and α is the ratio of exposures between the signal and background regions.

Following a similar derivation as above, we can obtain the so-called W statistics (Arnaud et al., 2022):

$$\mathcal{W} \equiv -2 \ln \mathcal{L} = 2 \sum_{i=1}^{N} [N_{\mathrm{pred},i} + (1+\alpha)\, b_i - N_{\mathrm{on},i} \ln(N_{\mathrm{pred},i} + \alpha\, b_i) - N_{\mathrm{off},i} \ln b_i] \ . \tag{B.6}$$

If there is no specific model for b_i, we can use the fact that the derivative of $\mathcal{L}$ with respect to B_i at the best fit is zero. Solving this equation leads to the expression for the expected background counts:

$$b_i = \frac{C + \sqrt{C^2 + 4\alpha\,(1+\alpha)\, N_{\mathrm{off},i} N_{\mathrm{pred},i}}}{2\alpha\,(1+\alpha)} \ , \tag{B.7}$$

with

$$C = N_{\mathrm{on},i} + \alpha\, N_{\mathrm{off},i} - (1+\alpha)\, N_{\mathrm{pred},i} \ . \tag{B.8}$$

Based on the W statistics, we can fit a spectral model to our reduced dataset, more precisely, fitting the predicted distribution N_{pred} to the measured excess count distribution in the reconstructed energy space. To determine the best-fit parameters, we need to maximize the joint likelihood $\mathcal{L}$, or equivalently, minimize $\mathcal{W}$. In Gammapy, this optimization process can be performed using `Fit` class, which works with different backends, including `iminuit` (Dembinski et al., 2020) as the default minimizer.

Appendix C

The ill-posed problem

The ill-posed nature limits the performance of direct fitting of the stepped power law model. This can be understood in the following mathematical way (see Wittek (2006) for more detailed discussions).

The fitting procedure is analogous to solving a set of equations:

$$A_i = \sum_{j=1}^{n_b} \mathbf{M}_{ij} \cdot B_j \quad (i = 1, \ldots, n_a) \ , \tag{C.1}$$

where A_i is the measured excess counts in the i-th reconstructed energy bin, B_j is the predicted counts in the j-th true energy bin, and $\mathbf{M}$ is the migration matrix with dimensions $n_a \times n_b$.

There are three cases for the solution B:

If $n_a > n_b$, the number of equations is larger than the number of unknown parameters, and the system is over-constrained. For Gaussian statistics, we can use the least square method to obtain the solution for B by minimizing

$$\chi_0^2 = (A - \mathbf{M}B)^T \cdot \mathbf{C_A^{-1}} \cdot (A - \mathbf{M}B) \ , \tag{C.2}$$

where $\mathbf{C_A}$ is the covariance matrix of measured distribution.

The best-fit B given by $\frac{\partial \chi_0^2}{\partial B} = 0$ will depend on $\mathbf{C_A}$:

$$B = (\mathbf{M}^T \mathbf{C_A^{-1}} \mathbf{M})^{-1} \mathbf{M}^T \mathbf{C_A^{-1}} A \ . \tag{C.3}$$

If $n_a = n_b$, we have a unique solution:

$$B = \mathbf{M}^{-1} A \ . \tag{C.4}$$

If $n_a < n_b$, the system is under-constrained. The general solution can be written as

$$B = B_0 + B_\perp \ , \tag{C.5}$$

where $B_\perp$ is the set of solutions to $\mathbf{M} \cdot B_\perp = 0$, and B_0 is a particular solution, given by

$$B_0 = \mathbf{M}^T (\mathbf{M} \cdot \mathbf{M}^T)^{-1} A \ . \tag{C.6}$$

To further consider the influence of the noise component of A, let's first introduce the Gram matrix $\mathbf{G}$, whose entries are the inner products of the row vectors of matrix $\mathbf{M}$

$$\mathbf{G} \equiv \mathbf{M} \cdot \mathbf{M}^T \ . \tag{C.7}$$

It can be proved that the Gram matrix is symmetric and positive semi-definite. Thus, we can decompose it into

$$\mathbf{G} = \mathbf{U} \mathbf{\Lambda} \mathbf{U}^T = \sum_{l=1}^{n_a} \lambda_l \, (u_l \cdot u_l^T) \ , \tag{C.8}$$

where $\mathbf{\Lambda}$ is a diagonal matrix of the eigenvalues λ_l, and $\mathbf{U}$ is an orthogonal matrix of the eigenvectors u_l.

Then the particular solution becomes

$$B_0 = \mathbf{M}^T \, [\sum_{l=1}^{n_a} \frac{1}{\lambda_l} (u_l \cdot u_l^T) \,] A \ . \tag{C.9}$$

The noise component of A, denoted as δA, will transform into B_0:

$$\delta B_0 = \mathbf{M}^T \, [\sum_{l=1}^{n_a} \frac{1}{\lambda_l} (u_l \cdot u_l^T) \,] \delta A \ . \tag{C.10}$$

This equation shows that the small eigenvalues of $\mathbf{G}$ will enhance the noise component of A, resulting in large noise component of B_0.

The covariance matrix of B will be

$$\mathbf{C_B} \equiv \delta B_0 \cdot (\delta B_0)^T = \mathbf{M}^T \, [\sum_{l=1}^{n_a} \frac{1}{\lambda_l} (u_l \cdot u_l^T) \,] \, \mathbf{C_A} \, [\sum_{k=1}^{n_a} \frac{1}{\lambda_k} (u_k \cdot u_k^T) \,] \, \mathbf{M} \ . \tag{C.11}$$

which implies that the correlations between adjacent bins in B are also enhanced by the small eigenvalues of $\mathbf{G}$.

To suppress the noise components and reduce the correlations induced by the noise, a regularization method can be introduced.

Appendix D

Software repository

In this thesis, I developed an MCMC technique with Tikhonov regularization for flux point estimation with `Gammapy`. Based on the stepped power law model proposed in Sec. 3.4.2, it addresses the issues in Gammapy's standard estimator `FluxPointEstimator` (see Sec. 3.4.1). The Tikhonov regularization term is further introduced to solve the ill-posed nature of the problem, which limits the performance of direct fitting of the stepped power law model. The theoretical framework for this novel method is described in Sec. 3.4.3.

The codes are publicly available in the following git repository:

https://github.com/Yunhe-Wang0/Gammapy_analysis.git

Bibliography

A. A. Abdo et al. Pulsed Gamma-rays from PSR J2021+3651 with the Fermi Large Area Telescope. *Astrophys. J.*, 700:1059–1066, 2009.

A. A. Abdo et al. Fermi Large Area Telescope Observations of the Crab Pulsar And Nebula. , 708(2):1254–1267, 2010a.

A. A. Abdo et al. Fermi LAT observations of the Geminga pulsar. *Astrophys. J.*, 720:272, 2010b.

A. A. Abdo et al. The Vela Pulsar: Results from the First Year of Fermi LAT Observations. *Astrophys. J.*, 713:154–165, 2010c.

A. A. Abdo et al. Fermi LAT observations of the Geminga pulsar. *Astrophys. J.*, 720:272, 2010d.

A. A. Abdo et al. The Second Fermi Large Area Telescope Catalog of Gamma-ray Pulsars. *Astrophys. J. Suppl.*, 208:17, 2013.

S. Abdollahi et al. *Fermi* Large Area Telescope Fourth Source Catalog. *Astrophys. J. Suppl.*, 247(1):33, 2020.

S. Abe et al. Standardised formats and open-source analysis tools for the MAGIC telescopes data. *JHEAp*, 44:266–278, 2024.

M. L. Ahnen et al. Search for VHE gamma-ray emission from Geminga pulsar and nebula with the MAGIC telescopes. , 591:A138, 2016.

A. Albert et al. Spectrum and Morphology of the Very-high-energy Source HAWC J2019+368. *Astrophys. J.*, 911(2):143, 2021.

J. Aleksić et al. The major upgrade of the MAGIC telescopes, Part I: The hardware improvements and the commissioning of the system. *Astropart. Phys.*, 72:61–75, 2016.

E. Aliu et al. Observation of pulsed gamma-rays above 25 GeV from the Crab pulsar with MAGIC. *Science*, 322:1221–1224, 2008.

E. Aliu et al. Spatially Resolving the Very High Energy emission from MGRO J2019+37 with VERITAS. *Astrophys. J.*, 788:78, 2014.

E. Aliu et al. A Search for Pulsations from Geminga Above 100 GeV with VERITAS. *Astrophys. J.*, 800(1):61, 2015.

K. Arnaud, C. Gordon, B. Dorman, and K. Rutkowski. Appendix B: Statistics in XSPEC, 2022. URL `https://heasarc.gsfc.nasa.gov/xanadu/xspec/manual/XSappendixStatistics.html`.

P. Auger, P. Ehrenfest, R. Maze, J. Daudin, and R. A. Fréon. Extensive cosmic-ray showers. *Rev. Mod. Phys.*, 11:288–291, 1939. URL `https://link.aps.org/doi/10.1103/RevModPhys.11.288`.

W. Baade and F. Zwicky. Remarks on Super-Novae and Cosmic Rays. *Physical Review*, 46(1):76–77, 1934.

D. C. Backer and R. W. Hellings. Pulsar timing and general relativity. , 24:537–575, 1986.

K. Bennett, G. F. Bignami, M. Bonnardeau, R. Buccheri, W. Hermsen, G. Kanbach, G. G. Lichti, H. A. Mayer-Hasselwander, J. A. Paul, L. Scarsi, R. Stiglitz, B. N. Swanenburg, and R. D. Wills. COS-B observations of localised high-energy gamma-ray emission from the anticentre region of the galactic disc. , 56(3):469–471, 1977.

D. L. Bertsch, K. T. S. Brazier, C. E. Fichtel, R. C. Hartman, S. D. Hunter, G. Kanbach, D. A. Kniffen, P. W. Kwok, Y. C. Lin, and J. R. Mattox. Pulsed high-energy γ-radiation from Geminga (1E0630+178). , 357(6376):306–307, 1992.

G. F. Bignami and P. A. Caraveo. Geminga: new period, old γ-rays. , 357(6376):287, 1992.

G. F. Bignami, P. A. Caraveo, and R. C. Lamb. An identification for "GEMINGA" (2CG 195+04) 1E 0630+178 : a unique object in the error box of the high-energy gamma-ray source. , 272:L9–L13, 1983.

A. Biland, M. Garczarczyk, H. Anderhub, V. Danielyan, D. Hakobyan, E. Lorenz, and R. Mirzoyan. The Active Mirror Control of the MAGIC Telescopes. In *International Cosmic Ray Conference*, volume 3 of *International Cosmic Ray Conference*, pages 1353–1356, 2008.

O. Blanch and A. Moralejo. How to use the camera simulation program 0.7, September 2004. URL `https://magic.mpp.mpg.de/backend/tdas-notes`. Internal MAGIC-TDAS note 04-07.

D. Borla Tridon, F. Goebel, D. Fink, W. Haberer, J. Hose, C. C. Hsu, T. Jogler, R. Mirzoyan, R. Orito, O. Reimann, P. Sawallisch, J. Schlammer, T. Schweizer, B. Steinke, and M. Teshima. Performance of the Camera of the MAGIC II Telescope. *arXiv e-prints*, art. arXiv:0906.5448, 2009.

R. Brun and F. Rademakers. ROOT: an object oriented data analysis framework. *Nucl. Instrum. Meth. A*, 389:81–86, 1997.

R. Buccheri, K. Bennett, G. F. Bignami, J. B. G. M. Bloemen, V. Boriakoff, P. A. Caraveo, W. Hermsen, G. Kanbach, R. N. Manchester, J. L. Masnou, H. A. Mayer-Hasselwander, M. E. Özel, J. A. Paul, B. Sacco, L. Scarsi, and A. W. Strong. Search for pulsed γ-ray emission from radio pulsars in the COS-B data. , 128:245–251, 1983.

P. A. Caraveo, A. De Luca, S. Mereghetti, A. Pellizzoni, and G. F. Bignami. Phase-Resolved Spectroscopy of Geminga Shows Rotating Hot Spot(s). *Science*, 305(5682): 376–380, 2004.

W. Cash. Parameter estimation in astronomy through application of the likelihood ratio. *Astrophys. J.*, 228:939–947, 1979.

G. Ceribella. *Insights into the 10-100 GeV gamma-ray emission of pulsars from extensive observations of MAGIC*. PhD thesis, Munich, Tech. U., 2021.

B. Cerutti, A. A. Philippov, and A. Spitkovsky. Modelling high-energy pulsar light curves from first principles. *Monthly Notices of the Royal Astronomical Society*, 457(3):2401–2414, 2016.

K. S. Cheng, C. Ho, and M. Ruderman. Energetic Radiation from Rapidly Spinning Pulsars. I. Outer Magnetosphere Gaps. , 300:500, 1986.

I. Contopoulos, D. Kazanas, and C. Fendt. The Axisymmetric Pulsar Magnetosphere. , 511(1):351–358, 1999.

J. K. Daugherty and A. K. Harding. Gamma-Ray Pulsars: Emission from Extended Polar CAP Cascades. , 458:278, 1996.

F. Dazzi, T. Schweizer, G. Ceribella, D. Corti, A. Dettlaff, J. R. Garcia, D. Häfner, D. Herranz, M. López-Moya, M. Mariotti, R. Maier, S. Metz, R. Mirzoyan, D. Nakajima, T. Saito, M. Shayduk, J. Sitarek, D. Strom, M. Teshima, S. Tran, and M. Will. The stereoscopic analog trigger of the magic telescopes. *IEEE Transactions on Nuclear Science*, 68(7):1473–1486, 2021.

O. C. de Jager and I. Büsching. The H-test probability distribution revisited: improved sensitivity. , 517:L9, 2010.

H. Dembinski, P. Ongmongkolkul, et al. scikit-hep/iminuit. Zenodo, 2020.

R. Dodson, D. Legge, J. E. Reynolds, and P. M. McCulloch. The Vela Pulsar's Proper Motion and Parallax Derived from VLBI Observations. , 596(2):1137–1141, 2003.

A. Donath et al. Gammapy: A Python package for gamma-ray astronomy. *Astron. Astrophys.*, 678:A157, 2023.

M. Doro, D. Bastieri, A. Biland, F. Dazzi, L. Font, M. Garczarczyk, M. Ghigo, E. Giro, F. Goebel, R. Kosyra, E. Lorenz, M. Mariotti, R. Mirzoyan, L. Peruzzo, G. Pareschi, and J. Zapatero. The reflective surface of the MAGIC telescope. *Nuclear Instruments and Methods in Physics Research A*, 595(1):200–203, 2008.

C. E. Fichtel, R. C. Hartman, D. A. Kniffen, D. J. Thompson, G. F. Bignami, H. Ögelman, M. E. Özel, and T. Tümer. High-energy gamma-ray results from the second Small Astronomy Satellite. , 198:163–182, 1975.

J. M. Fierro, P. F. Michelson, P. L. Nolan, and D. J. Thompson. Phase-resolved Studies of the High-Energy Gamma-Ray Emission from the Crab, Geminga, and VELA Pulsars. , 494(2):734–746, 1998.

V. P. Fomin, A. A. Stepanian, R. C. Lamb, D. A. Lewis, M. Punch, and T. C. Weekes. New methods of atmospheric Cherenkov imaging for gamma-ray astronomy. I. The false source method. *Astroparticle Physics*, 2(2):137–150, 1994.

P. Goldreich and W. H. Julian. Pulsar Electrodynamics. , 157:869, 1969.

A. Gruzinov. Power of an axisymmetric pulsar. *Phys. Rev. Lett.*, 94:021101, 2005.

C. Guépin, B. Cerutti, and K. Kotera. Proton acceleration in pulsar magnetospheres. , 635:A138, 2020.

J. P. Halpern and S. S. Holt. Discovery of soft X-ray pulsations from the γ-ray source Geminga. , 357(6375):222–224, 1992.

J. P. Halpern, F. Camilo, A. Giuliani, E. V. Gotthelf, M. A. McLaughlin, R. Mukherjee, A. Pellizzoni, S. M. Ransom, M. S. E. Roberts, and M. Tavani. Discovery of High-Energy Gamma-Ray Pulsations from PSR J2021+3651 with AGILE. *Astrophys. J. Lett.*, 688: L33, 2008.

D. Heck, J. Knapp, J. N. Capdevielle, G. Schatz, and T. Thouw. *CORSIKA: a Monte Carlo code to simulate extensive air showers.* 1998.

W. Hermsen, B. N. Swanenburg, G. F. Bignami, G. Boella, R. Buccheri, L. Scarsi, G. Kanbach, H. A. Mayer-Hasselwander, J. L. Masnou, and J. A. Paul. New high energy gamma-ray sources observed by COS B. , 269:494–495, 1977.

H.E.S.S. Collaboration. First Ground-based Measurement of Sub-20 GeV to 100 GeV γ-rays from the Vela Pulsar with H.E.S.S. II. *Astron. Astrophys.*, 620:A66, 2018.

J. W. T. Hessels, M. S. E. Roberts, S. M. Ransom, V. M. Kaspi, R. W. Romani, C. Y. Ng, P. C. C. Freire, and B. M. Gaensler. Observations of PSR J2021+3651 and its x-ray pulsar wind nebula G75.2+0.1. *Astrophys. J.*, 612:389–397, 2004.

A. Hewish, S. J. Bell, J. D. H. Pilkington, P. F. Scott, and R. A. Collins. Observation of a Rapidly Pulsating Radio Source. , 217(5130):709–713, 1968.

A. M. Hillas. Cerenkov Light Images of EAS Produced by Primary Gamma Rays and by Nuclei. In F. C. Jones, editor, *19th International Cosmic Ray Conference (ICRC19), Volume 3*, volume 3 of *International Cosmic Ray Conference*, page 445, 1985.

K. Ishio. *Improvement in the gamma-ray energy reconstruction of MAGIC and impact on the spectral analysis of the first Gamma Ray Burst detected at TeV energies*. PhD thesis, Ludwig-Maximilians-Universität München, 2020.

M. S. Jackson, J. P. Halpern, E. V. Gotthelf, and J. R. Mattox. A High-Energy Study of the Geminga Pulsar. , 578(2):935–942, 2002.

C. Kalapotharakos, G. Brambilla, A. Timokhin, A. K. Harding, and D. Kazanas. Three-dimensional Kinetic Pulsar Magnetosphere Models: Connecting to Gamma-Ray Observations. , 857(1):44, 2018.

A. Kirichenko, A. Danilenko, P. Shternin, Y. Shibanov, E. Ryspaeva, D. Zyuzin, M. Durant, O. Kargaltsev, G. Pavlov, and A. Cabrera-Lavers. Optical Observations of Psr J2021+3651 in the Dragonfly Nebula With the GTC. , 802(1):17, 2015.

L. Landau. On the theory of stars. *Physikalische Zeitschrift Sowjetunion*, 1:285–288, 1932.

T. P. Li and Y. Q. Ma. Analysis methods for results in gamma-ray astronomy. , 272: 317–324, 1983.

MAGIC Collaboration. Detection of the Geminga pulsar with MAGIC hints at a power-law tail emission beyond 15 GeV. *Astron. Astrophys.*, 643:L14, 2020.

R. N. Manchester, G. B. Hobbs, A. Teoh, and M. Hobbs. The Australia Telescope National Facility Pulsar Catalogue. , 129(4):1993–2006, 2005.

J. R. Mattox, D. L. Bertsch, C. E. Fichtel, R. C. Hartman, D. A. Kniffen, and D. J. Thompson. SAS 2 Observation of Pulsed High-Energy Gamma Radiation from Geminga. , 401:L23, 1992.

H. A. Mayer-Hasselwander, D. L. Bertsch, K. T. S. Brazier, J. Chiang, C. E. Fichtel, J. M. Fierro, R. C. Hartman, S. D. Hunter, G. Kanbach, P. W. Kwok, D. A. Kniffen, Y. C. Lin, J. R. Mattox, P. F. Michelson, P. L. Nolan, K. Pinkau, H. Rothermel, E. J. Schneid, M. Sommer, P. Sreekumar, D. J. Thompson, and C. von Montigny. High-Energy Gamma Radiation from Geminga Observed by EGRET. , 421:276, 1994.

R. Mirzoyan. On the Calibration Accuracy of Light Sensors in Atmospheric Cherenkov Fluorescence and Neutrino Experiments. In *International Cosmic Ray Conference*, volume 7 of *International Cosmic Ray Conference*, page 265, 1997.

T. Mizuno, N. Tanaka, H. Takahashi, J. Katsuta, K. Hayashi, and R. Yamazaki. X-Ray Studies of the Extended TeV Gamma-Ray Source VER J2019+368. , 841(2):104, 2017.

A. Moralejo. The reflector simulation program v.0.6, January 2003. URL `https://magic.mpp.mpg.de/backend/tdas-notes`. Internal MAGIC-TDAS note 02-11.

K. Mori, E. V. Gotthelf, F. Dufour, V. M. Kaspi, J. P. Halpern, A. M. Beloborodov, H. An, M. Bachetti, S. E. Boggs, F. E. Christensen, W. W. Craig, C. J. Hailey, F. A. Harrison, C. Kouveliotou, M. J. Pivovaroff, D. Stern, and W. W. Zhang. A Broadband X-Ray Study of the Geminga Pulsar with NuSTAR and XMM-Newton. , 793(2):88, 2014.

D. Nakajima, D. Fink, J. Hose, R. Mirzoyan, D. Paneque, K. Saito, T. Schweizer, M. Teshima, T. Toyama, and H. Wetteskind. New Imaging Camera for the MAGIC-I Telescope. In *International Cosmic Ray Conference*, volume 33 of *International Cosmic Ray Conference*, page 3044, 2013.

W. Pence. CFITSIO, v2.0: A New Full-Featured Data Interface. In D. M. Mehringer, R. L. Plante, and D. A. Roberts, editors, *Astronomical Data Analysis Software and Systems VIII*, volume 172 of *Astronomical Society of the Pacific Conference Series*, page 487, 1999.

W. D. Pence, Chiappetti, L., Page, C. G., Shaw, R. A., and Stobie, E. Definition of the Flexible Image Transport System (FITS), version 3.0. *AA*, 524:A42, 2010.

A. Philippov and M. Kramer. Pulsar Magnetospheres and Their Radiation. , 60:495–558, 2022.

M. S. E. Roberts, J. W. T. Hessels, S. M. Ransom, V. M. Kaspi, P. C. C. Freire, F. Crawford, and D. R. Lorimer. PSR J2021+3651: A Young Radio Pulsar Coincident with an Unidentified EGRET γ-Ray Source. , 577(1):L19–L22, 2002.

R. W. Romani. Gamma-Ray Pulsars: Radiation Processes in the Outer Magnetosphere. , 470:469, 1996.

B. Rossi. Misure sulla distribuzione angolare di intensita della radiazione penetrante all'asmara ("measurements on the angular distribution of the pene- tratingradiation-intensityinasmara"). *Supplemento a la Ricerca Scientifica*, 1:579, 1934.

M. A. Ruderman and P. G. Sutherland. Theory of pulsars: polar gaps, sparks, and coherent microwave radiation. , 196:51–72, 1975.

T. Saito and J. Sitarek. Improvement of the θ^2 analysis by using the random forest method in the disp estimation, May 2009. URL `https://magic.mpp.mpg.de/backend/tdas-notes`. Internal MAGIC-TDAS note 09-01.

M. Schmelling. The method of reduced cross entropy: a general approach to unfold probability distributions. *Nucl. Instrum. Meth. A*, 340:400–412, 1994.

M. Shayduk and C. Consortium. Optimized Next-neighbour Image Cleaning Method for Cherenkov Telescopes. In *International Cosmic Ray Conference*, volume 33 of *International Cosmic Ray Conference*, page 3000, 2013.

D. A. Smith et al. The Third Fermi Large Area Telescope Catalog of Gamma-Ray Pulsars. *Astrophys. J.*, 958(2):191, 2023.

D. Sobczynska. Mmcs from corsika 6.014, July 2002. URL `https://magic.mpp.mpg.de/backend/tdas-notes`. Internal MAGIC-TDAS note 02-10.

P. A. Sturrock. A Model of Pulsars. , 164:529, 1971.

D. J. Thompson. Gamma ray astrophysics: the EGRET results. *Rept. Prog. Phys.*, 71: 116901, 2008.

A. N. Tikhonov. On the solution of ill-posed problems and the method of regularization. *Dokl. Akad. Nauk SSSR*, 151:501–504, 1963.

A. N. Timokhin. On the force-free magnetosphere of an aligned rotator. *Monthly Notices of the Royal Astronomical Society*, 368(3):1055–1072, 2006. ISSN 0035-8711.

A. Van Etten, R. W. Romani, and C. Y. Ng. Rings and Jets around PSR J2021+3651: the 'Dragonfly Nebula'. *Astrophys. J.*, 680:1417, 2008.

R. M. Wagner. *Measurement of very high energy gamma-ray emission from four blazars using the MAGIC telescope and a comparative blazar study.* PhD thesis, Munich, Tech. U., 2006.

W. Wittek. Unfolding. Internal MAGIC-TDAS note 05-05, 2006. URL `https://magic.mpp.mpg.de/backend/tdas-notes`.

R. Zanin et al. MARS, the MAGIC analysis and reconstruction software. In *33rd International Cosmic Ray Conference*, page 0773, 2013.

Acknowledgments

First, I would like to sincerely thank my supervisor Gayoung Chon. Starting from the high energy astrophysics course, she has guided me to the exciting field of gamma-ray astronomy. She provided me the opportunity to do research in the MAGIC group at the MPP and learn the state-of-the-art gamma-ray pulsar observations. Along the way, she has always been there to offer help and support patiently, no matter how busy she is. She provided valuable comments on the structure and scientific results of this thesis. I wish I could have learned more from her.

I would like to give special thanks to Giovanni Ceribella, my 'day-by-day' supervisor. His guidance and help were throughout this work, from basic data processing to insightful discussions on the scientific results and pulsar physics. He taught me the skills of analyzing raw pulsar data step by step, and the pipeline itself has many of his contributions. He provided many valuable insights and instructions on our MCMC-based technique, not only the theoretical framework, but the coding process. He also helped me solve some tricky technical problems and revised this thesis in detail. I will always remember this wonderful journey of exploring gamma-ray pulsars together.

I would like to express my thanks to David Green for the helpful discussions on the MCMC technique with regularization. I received many expert opinions from him on the Gammapy flux point estimator and the development of this MCMC-based technique.

I would also like to say thank you to Giorgio Pirola for the friendly guidance. He helped me a lot in learning Gammapy.

I was also supported by Jan Lukas Schubert for the installation of MAGIC DL3 converter.

Lastly, I would like to thank the entire MAGIC group for the friendly support and encouragement.